Supplementary Materials for

The Petrochemistry of Jake_M: A Martian Mugearite

E. M. Stolper,* M. B. Baker, M. E. Newcombe, M. E. Schmidt, A. H. Treiman, A. Cousin, M. D. Dyar, M. R. Fisk, R. Gellert, P. L. King, L. Leshin, S. Maurice, S. M. McLennan, M. E. Minitti, G. Perrett, S. Rowland, V. Sautter, R. C. Wiens, MSL Science Team

*Corresponding author. E-mail: ems@gps.caltech.edu

Published 27 September 2013, Science **341**, 1239463 (2013)
DOI: 10.1126/science.1239463

This PDF file includes:

Materials and Methods
Supplementary Text
Figs. S1 to S24
MSL Science Team Author List
Full Reference List

Supplementary Text

Here we present supporting materials for the article: The Petrochemistry of Jake_M: A Martian Mugearite. In particular, we provide a more complete discussion and supporting figures (S1–S4) for the LIBS analyses. We also compare Jake_M (JM) to terrestrial igneous rocks and show the close compositional resemblance of JM to terrestrial mugearites and phonotephrites (Figs. S5, S6). We compare the composition of JM to the compositions of terrestrial lavas in terms of TiO_2 *vs*. MgO (Fig. S7) and Fe/Mn *vs*. MgO (Fig. S8). Data from (*10, 75, 76*) are also used to demonstrate how the SO_3 and Cl contents of "unbrushed" or "as is" rocks analyzed by the Mars Exploration Rovers (MERs) compare to the sulfur and chlorine contents of the "unbrushed" JM analyses (Fig. S9). We also compare unbrushed and physically abraded compositions from the same outcrops (both normalized to 100 wt. % on a SO_3- and Cl-free basis) analyzed by the Spirit rover to the three normalized JM analyses (Fig. S10) to demonstrate that, for a given rock/outcrop, the major element spread in the unbrushed and abraded analyses, once renormalized, is comparable to the spread in the three JM analyses. Additionally, we provide a more detailed discussion of the MELTS calculations as well as a complete set of oxide-MgO variation diagrams (for SiO_2, TiO_2, Al_2O_3, FeO*, CaO, Na_2O, K_2O, and P_2O_5) showing the Tenerife Island lavas, JM, and selected MELTS fractionation paths (Fig. S11). A contoured misfit map (Fig. S12) shows the extent to which MELTS calculations at different pressures and with varying initial water contents match the overall fractionation trend of the Tenerife lavas. A similar set of figures shows MELTS fractional crystallization calculations (in oxide-MgO space) and misfit contour maps where the starting compositions were various known martian rocks (surface rocks from Gusev Crater, and the NWA 7034 meteorite), both with and without arbitrarily increased Na_2O and K_2O contents (Figs. S13–S24). The purpose of these calculations was to test whether known martian rock compositions could be viable parental liquids for JM. At the end of the Supplement, we list all MSL science team members and their institutional affiliations.

We note that in two previously presented abstracts of oral presentations that discussed the petrogenesis of JM (*82, 83*), the JM composition was compared to lavas from St. Helena, and not those from Tenerife. These two abstracts were based on a preliminary APXS data reduction of the raw JM analyses. Following a re-calibration of the APXS data, the composition of JM changed slightly and although the average of the new and old analyses overlap at 2σ, the St. Helena fractionation trend was not as good a match to the revised JM composition as it had been to the previous composition. For this reason, the compositions of St. Helena lavas have been replaced in this work by lavas from Tenerife Island. Nevertheless, it is important to stress that both terrestrial suites are alkaline and

that the most successful MELTS calculations for both suites require moderate pressures and water contents.

Materials and Methods

Three APXS analyses of JM were obtained on two unbrushed areas ~1.7 cm in diameter (JM1 and JM2) and separated by ~7 cm (Fig. 1): JM1 was analyzed once during the day and JM2 was analyzed twice (at night and during the day). Results of the three analyses are listed in Table 1. The surface of JM was not brushed or abraded prior to analysis, so the APXS analyses include surface-correlated contributions, including adhering dust that likely contributes to the observed S and Cl. Note that Na and Mg would be the major elements most affected in the APXS analyses by surface-correlated components since most emitted X-rays for Na and Mg originate in the outer ~2 to 3 μm of the target (*71, 84*). However, experience with the MERs indicates that the characteristics of rock compositions are typically not obscured by surface components, and the levels of S in JM are lower than in most unbrushed analyses from the Exploration rovers (see The effect of surface components on Jake_M's composition below), so the level of surface contamination and alteration are likely relatively minor (*85*). Moreover, successive LIBS shots on a single location gave no evidence of a surface coating or crust, but suggested instead a thin dust layer that was penetrated within 1–2 laser shots (*3*). Individual LIBS shots involved a spot size of ~0.45 mm and a penetration depth of ~0.5 μm (*86, 87*). Although the differences between the JM1 and JM2n analyses (the two long-duration analyses; Table 1) are small in an absolute sense, none of the concentrations except Cr_2O_3 overlap at the 2σ level. This suggests heterogeneity on a cm scale—not unsurprising in a polymineralic igneous rock—and consistent with the observed variations between the LIBS analyses (albeit on a different length scale).

ChemCam Analyses

Fourteen locations were analyzed by ChemCam (*86, 87*) on JM with two sets of measurements (*3, 88*): a 5-point line-scan with points separated by ~6 mm on sol 45 while the target was at a distance of 3.8 m, and a 3×3 raster (total of 9 LIBS points separated by 7 mm horizontally and ~10 mm vertically) on sol 48 while the target was at a distance of 3.2 m (Figs. 1, S1). Thirty laser shots [spot size around 420-440 μm; (*89*)] were directed at each analysis location, each providing a spectrum at successive depths to a maximum depth of ~15 μm inside the rock (*87*). The 420 spectra obtained from the fourteen LIBS analysis locations show that JM is heterogeneous at scales > ~0.5 mm (and likely smaller), with the thirty spectra from each analysis location defining a separate compositional cluster in multi-dimensional component space. Four distinct end-member compositions were determined by subjecting 392 spectra (the first two spectra at each analysis location were excluded since they are most affected by surface dust) to an

independent component analysis (ICA) algorithm. ICA involves a linear transformation that minimizes the statistical dependence between components, allowing spectra to be compared in the phase space of the most strongly varying components (*90, 91*). Different components can represent the spectral signature of a single element. Plots displaying ICA results show the correlation coefficients of the represented elements in arbitrary units. Figure S2 shows the Ti component versus the Ca component obtained from ICA. Most of the 28 spectra from each analysis location cluster together showing that for these elements the composition does not vary significantly with depth. We observe two main end members corresponding to analysis locations 1 and 2 (labeled JM_1 and JM_2 in Fig. S2). JM_2 is strongly associated with Ti, whereas JM_1 shows the lowest Ca. The other two end members are also labeled in Fig. S2: JM_10 is enriched in alkali elements (Fig. S3), whereas JM_14 shows higher Ca.

Figure S3 presents the four end members in the ultra-violet (UV) and part of the visible and near infrared (VNIR) spectral ranges. For this figure, the spectra from each analysis location were averaged over depth, which is justified in most cases given the similarity of most analysis points. Ti line intensities are low in JM_1 and JM_10. JM_1 and JM_2 (in red and green, respectively) also show weak Ca lines compared to JM_10 and JM_14 (in blue and black, respectively). JM_1 and JM_14 show stronger Mg signals than JM_2. This location (JM_2) shows almost no Mg, Al, and Ca, and is interpreted to be a mixture that includes Fe-Ti oxide(s). JM_10 is enriched in Al and alkalis relative to JM_2 and JM_14. Preliminary elemental compositions in wt. % were obtained via the partial-least-square (PLS) technique discussed by Lasue et al. (*92*); these compositions are consistent with three major types of minerals: plagioclase, pyroxene, and olivine. PLS also shows that JM-2 does not contain a significant fraction of these three phases—its higher Fe and Ti are consistent with a substantial fraction of Fe-Ti oxide(s) in the analyzed volumes of each laser shot.

While most of the JM analysis locations are homogeneous with depth, a comparison of the thirty successive spectra at each analysis location shows that some locations exhibit significant heterogeneity with increasing depth. The location showing the greatest heterogeneity with depth is JM_14. Figure S4a shows that successive spectra at this location have increasing MgO and CaO along a linear trend. The first two shots (Fig. S4a) are contaminated by dust, and then the trend (shots 3–30) suggests a mixture of groundmass (?) and plagioclase and high-Ca pyroxene with the proportion of pyroxene increasing with depth. The presence of groundmass is suggested by CIPW normative components such as orthoclase, pyroxene, magnetite and ilmenite in the composition from shot number 4. A CIPW norm calculation of the 30^{th} laser shot composition contains > 50% diopside+hedenbergite but the analysis is potentially consistent, within uncertainties, with other Ca-rich pyroxene compositions. Figure S4b shows the same

location for other elements, indicating that they are decreasing in a manner consistent with progressive profiling into a region that is dominated by a high-Ca pyroxene grain but with other contributions to the spectra. This result indicates that JM contains mineral grains that are at least nearly as large as the laser beam diameter. Other locations generally show less variation with depth, although JM_4 initially shows a composition enriched in CaO and MgO, which becomes richer in alkalis at greater depth. This trend suggests that in this case, first a pyroxene was sampled, and then the fine-grained matrix.

Further Compositional Comparisons of Jake_M to Terrestrial Lavas

Figures S5 and S6 compare the three JM analyses (normalized to 100% minus SO_3, Cl, and trace elements) to rock compositions culled from the Georoc database that had been labeled either as mugearites or phonotephrites. With the exception of TiO_2-MgO and Na_2O-MgO, the JM compositions plot broadly near the centers of the remaining oxide-MgO mugearite fields (Fig. S5). For TiO_2 and Na_2O, JM lies near/on the lower and upper boundaries of the range of mugearite compositions, respectively. Similarly, the JM compositions lie at the extreme ranges of Na_2O (upper bound) and TiO_2 (lower bound) of rocks called phonotephrites (Fig. S6). But unlike the mugearites, JM's K_2O content is much lower than typical phonotephrites. It is largely for these reasons that, although JM plots in the phonotephrite field in the total alkali-silica diagram in Fig. 2 (although near the phonotephrite/mugearite boundary), we prefer to refer to it as a mugearite, since it has a stronger overall affinity to terrestrial rocks that have been given this designation.

As noted in the main text, martian rocks are depleted in TiO_2 relative to alkaline lavas from the island of Tenerife. However, Fig. S7 shows that, although they are low, the TiO_2 contents of JM, basaltic shergotittes (martian meteorites) and martian rocks analyzed by the Mars Exploration Rovers, are not outside of the range of both terrestrial alkaline lavas and terrestrial tholeiites. In Fig. S7a, the JM compositions plot at the lower end, but nevertheless within the range of TiO_2 contents in alkaline lavas with similar MgO and SiO_2 contents. Likewise, JM, basaltic shergotittes, and Mars surface rocks are not outside of the TiO_2-MgO field defined by terrestrial tholeiites (Fig. S7b).

Although bulk rock Fe/Mn ratios have historically been one of the criteria used to distinguish martian from terrestrial rocks, (e.g., *29, 30*), Fig. S8 shows that the long-duration nighttime analysis of JM has Fe/Mn and MgO values that place it on the trend of Tenerife lavas in Fe/Mn-MgO space. High-precision Fe/Mn measurements (*93, 94*) of Hawaiian and Icelandic lavas with MgO contents of ~7–28 wt. % have values between ~58 and 70; these values are largely independent of MgO and are substantially above the JM value of 53. Fe/Mn values of Tenerife lavas with > ~7–8 wt. % MgO, although displaying greater variation (~90% of the lavas with >8 wt. % MgO have Fe/Mn of 60–80), nevertheless overlap the high-precision measurements on Hawaiian and Icelandic

basalts (greater scatter in Fe/Mn among the Tenerife rocks largely reflects lower precision of the MnO measurements). However, at lower magnesium contents (< ~7–8 wt. % MgO), Fe/Mn values in the Tenerife lavas are positively correlated with MgO and drop dramatically reaching values as low as 10–15 at MgO < 1 wt. %. This drop in Fe/Mn reflects the appearance and fractionation of titanomagnetite (± ilmenite) at MgO contents < ~7–8 wt. % and is consistent with the MELTS models in which Fe-rich spinel appears in the liquid-line-of-descent at ~7–8 wt. % MgO (Fig. 4, S11). Although not plotted, we note that lavas from St. Helena show a similar monotonic decrease in Fe/Mn with decreasing magnesium content once bulk rock MgO values fall below ~7–8 wt. %. Note that the martian rocks plotted in Fig. S8 have Fe/Mn values that are essentially independent of MgO content (~4–22 wt. %) and thus for MgO concentrations > ~6–7 wt. %, Fe/Mn values (~30–45) are substantially below the terrestrial ratios. However, because Fe/Mn values are not positively correlated with MgO at low MgO contents, more evolved (i.e., less magnesian) martian rocks intersect the Tenerife trend, suggesting that Fe/Mn is not a robust discriminant for evolved martian and terrestrial lavas.

The Effect of Surface Components on Jake_M's Composition

As discussed in the main text and in the Materials and Methods section above, the surface of Jake_M was not cleaned (i.e., mechanically brushed or physically abraded) prior to the three APXS analyses and thus a major fraction of the S and Cl in the analyses may reflect a surface component such as dust. Figure S9 compares SO_3 and Cl contents in JM with those from rocks analyzed by the MERs. With respect to S, the JM concentrations are lower than in most of the martian rock analyses collected from undisturbed (i.e., "as is") surfaces; in fact only a few rocks have lower S contents (e.g., Backstay, Irvine, Esperanza, and Humboldt Peak). Cl contents in the analyses of JM are roughly at the mid-point of the range of Cl concentrations in "as is" rock analyses (~0.4–1.6 wt. % Cl). Figure 10 shows that the spread in SiO_2, Al_2O_3, FeO*, CaO and MgO concentrations among the three normalized JM analyses is comparable to the spread observed in analyses of "as is" *vs*. abraded rock/outcrop surfaces once each analysis had been normalized on a SO_3- and Cl-free basis. This suggests that if we had analyses of JM from an abraded surface, they would not be sufficiently different from the compositions in Table 1 (once all had been renormalized without S and Cl) to substantively change any of the conclusions of this study.

MELTS Modeling of Liquid-lines-of-descent: Tenerife

AlphaMELTS 1.2 (*39, 40*) was used to model fractional crystallization of a primitive Tenerife composition (all in wt. %: SiO_2 44.231; TiO_2 3.186; Al_2O_3 11.317; Cr_2O_3 0.098; FeO* 12.431; MnO 0.181; MgO 12.672; CaO 12.430; Na_2O 2.253; K_2O 0.801; P_2O_5 0.401), over a range of pressures (1 bar and 1, 2, 3, 4, and 6 kbar) and starting water concentrations (0, 0.1, 0.5, 1, 2, and 3 wt. %). The effect of oxygen fugacity (fO_2) on the

liquid-lines-of-descent was also explored; however, a fixed fO_2 of QFM+1 is shown in Figs. S11 and S12. This fO_2 is consistent with estimates from Fe-Ti oxides in Tenerife volcanics (*38*); under more oxidizing or reducing conditions Fe-rich spinel would appear earlier or later in the calculated liquid-line-of-descent. For each fractional crystallization calculation, the oxides were plotted against MgO and cubic spline functions were fit to the discrete model points. The Tenerife lavas and a subset of MELTS calculations are shown in Fig. S11. For each of the 36 MELTS calculations, a misfit parameter was calculated by summing the absolute values of the differences between the MELTS curves in SiO_2-, Al_2O_3-, FeO*-, and CaO-MgO space and the Tenerife lava compositions; i.e., for each Tenerife lava, the MgO concentration was used to calculate an SiO_2, Al_2O_3, FeO*, and CaO content based on cubic spline fits to a given MELTS calculation and the absolute value of these differences were summed for all of the lavas with MgO contents between 1 and 12.685 wt. %. The sum of the differences was then divided by the number of Tenerife data points in this composition range (445). Some of the calculated liquid-lines-of-descent at pressures > 1 kbar and water concentrations < 2 wt. % became saturated in orthopyroxene at low MgO concentrations (MgO < 2.5 wt. %). Orthopyroxene is not expected in evolved alkaline magmas, (e.g., *16*) and has not been observed in the Tenerife lavas (e.g., *95*), so the crystallization of this phase was suppressed for the calculations shown in Figs. S11 and S12 [we note that MELTS is known to overstabilize orthopyroxene and thus its presence in these calculated evolved liquid compositions is likely an artifact (*96*)].

Figure S12 shows a contour plot of misfit over the tested range of pressures and water concentrations. The best fit over this range of pressures and water concentrations is in the middle of the darkest blue region at a pressure of 4 kbar and a starting water concentration of 1 wt. %. As illustrated by the MgO variation diagrams in Fig. S11, a good match to the Tenerife data requires the suppression of plagioclase crystallization such that the Al_2O_3 concentrations in the most evolved melts can be enriched to ~20 wt. %. Although the "best-fit" requires elevated pressure and water contents, as discussed in the main text, the suppression of plagioclase can be achieved by increasing the pressure of crystallization either with or without added water (increasing pressure and water content is more effective than pressure alone).

MELTS Modeling of Liquid-lines-of-descent: Martian Starting Liquid Compositions

We explored the possibility that JM might represent a residual liquid from fractional crystallization of known martian rock compositions. We tried a variety of starting liquid compositions, including the shergottite EETA 79001A (*9*), NWA 7034 (*74*), and four compositions measured by the Spirit rover in Gusev crater: Adirondack, Humphrey, Humboldt Peak, and Backstay. For these starting compositions, we again used MELTS to calculate liquid-lines-of-descent over a range of pressures (1 bar and 1, 2, 3, and 4 kbar)

and starting water concentrations (0, 0.1, 0.5, 1, 2, and 3 wt. %). We tried calculations over a range of fO_2 conditions from QFM−1 to QFM+3 (*6, 7, 97*). However, all of the results shown in Figs. S13–S24 were calculated at QFM−1. The misfit between the calculated liquid-lines-of-descent and JM was computed using a similar method to that described above for Tenerife, the only difference being that the calculated concentrations of SiO_2, Al_2O_3, FeO*, and CaO were this time compared to the three analyses of JM instead of the large Tenerife dataset. The results of the Backstay, NWA 7034, and Humboldt Peak calculations are discussed below.

Although none of the martian compositions considered in this study have high enough concentrations of alkalis to be viable parental liquids for JM (Figs. S13, S17, and S21), fractional crystallization of Backstay is able to match the concentrations of SiO_2, Al_2O_3, FeO*, and CaO in JM reasonably well (Fig. S13). A contoured misfit plot using Backstay as the starting composition (Fig. S14) shows that the best-fit conditions are 4 kbar and 3 wt. % water in the starting composition. These conditions yield a best-fit match to JM that is comparable to the best-fit to JM achieved by starting with the primitive Tenerife composition (again considering only SiO_2, Al_2O_3, FeO*, and CaO). However, all of the melts comprising the best-fit liquid-line-of-descent calculated using Backstay are hyperthene normative (i.e., normative nepheline = 0), in striking contrast to the ~16–17 wt. % normative nepheline in the JM bulk composition (Table 1).

Fractional crystallization of NWA 7034 and Humboldt Peak give poorer fits to JM (in terms of SiO_2, Al_2O_3, FeO*, and CaO) than Backstay, with misfits ranging from 7.5–12 for NWA 7034 (Fig. S18) and 10.5–12 for Humboldt Peak (Fig. S22). However, unlike Backstay, NWA 7034 and Humboldt Peak produced fractionated model liquids in the compositional region of JM (~4.4 wt. % MgO) that are nepheline normative, although the calculated abundances of normative nepheline (< 1 wt. %, NWA 7034; ~6 wt. % Humboldt Peak) are substantially less than that calculated for JM (~16–17 wt. %). In addition to having insufficient alkalis, both NWA 7034 and Humboldt Peak have concentrations of Al_2O_3 that are too low and concentrations of FeO* that are too high for either of these starting compositions to be parental to JM under the conditions considered in this study.

In order to assess whether a known martian composition enriched in alkalis could provide a viable parent for JM, we re-calculated the liquid-lines-of-descent from Backstay, NWA 7034, and Humboldt Peak with arbitrarily increased concentrations of Na_2O and K_2O. The addition of extra alkalis had the effect of decreasing the Al_2O_3 and SiO_2 concentrations of the residual liquids at a given MgO concentration, which increased the combined misfit for SiO_2, Al_2O_3, FeO*, and CaO between the calculated liquid-lines-of-descent and JM (Figs. S16, S20, and S24). The best-fit conditions for the Backstay

starting composition shifted to a higher pressure and a lower water concentration as a result of increasing the alkali concentration of the melt. This could reflect the role of Na_2O and K_2O as network modifiers in silicate liquids (*98*).

In conclusion, of the martian starting compositions considered in this study, fractional crystallization of Backstay provides the best match to the SiO_2, Al_2O_3, FeO*, and CaO concentrations in JM. However, concentrations of K_2O and Na_2O for all previously analyzed martian rocks, including Backstay, are too low to explain the alkali-rich nature of JM. A Backstay-like melt arbitrarily enriched in alkalis could on fractionation produce a melt similar to JM in most elements via fractional crystallization. The best-fit crystallization conditions are at pressures of 3 kbar or higher for all starting melt compositions.

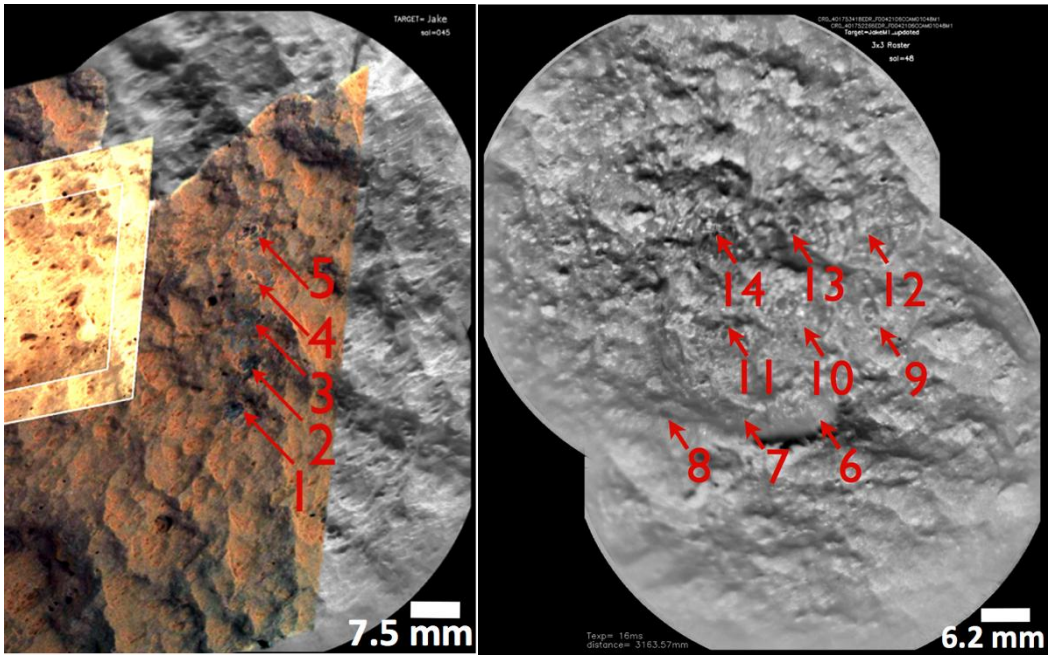

Fig. S1.

RMI mosaics of the 2 rasters performed on Jake_M. The mosaic on the left is coupled with Mahli colors. Credit : NASA/JPL-Caltech/ LANL/IRAP/MSSS/IAS/LTP- Nantes.

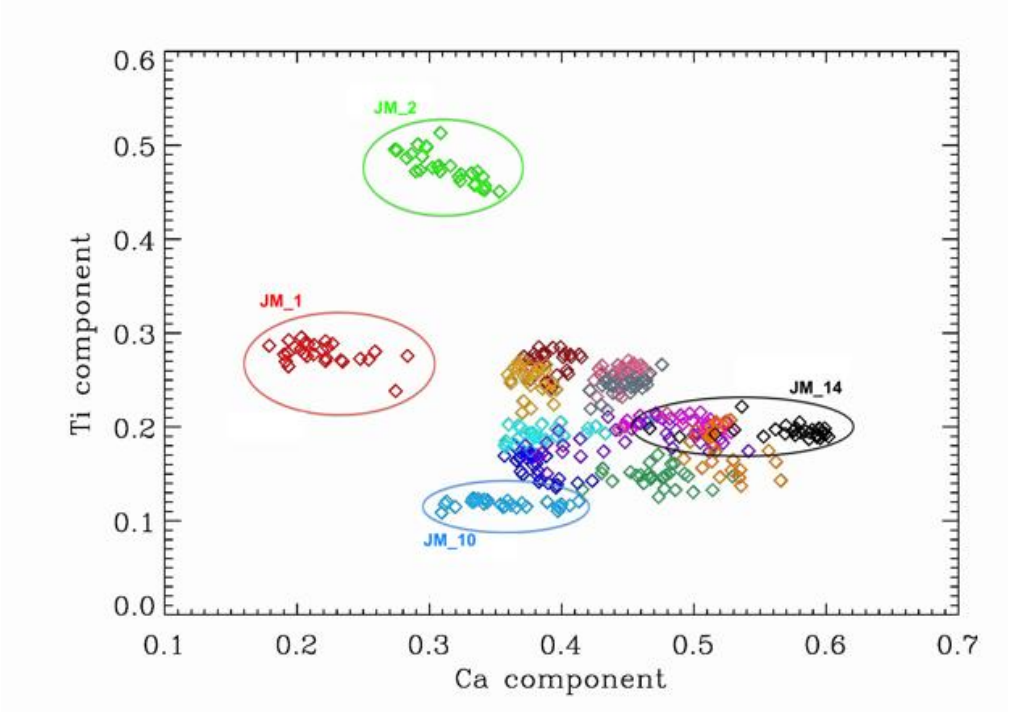

Fig. S2.

ICA (*91*) plot showing Ti component *vs*. Ca component for all the 392 spectra obtained on Jake_M (dust spectra removed). Observations at locations 1, 2, 10, and 14 represent compositional end-members. Units along the axes give relative separation of a given ICA component.

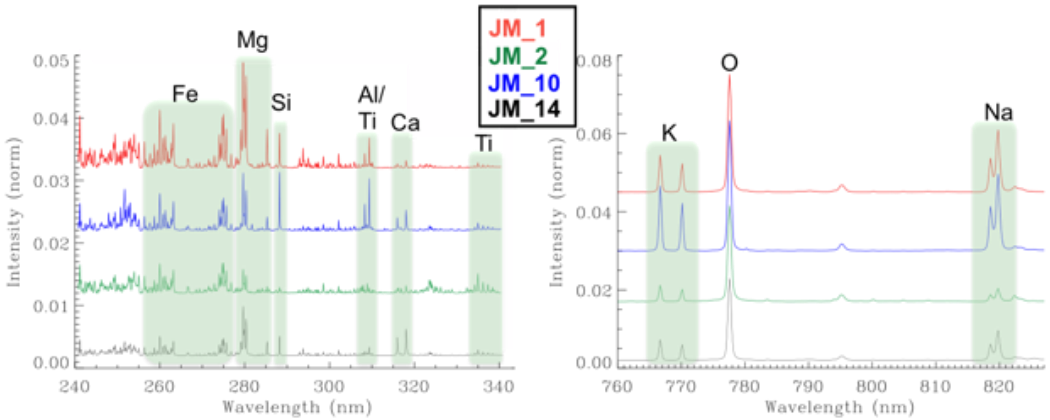

Fig. S3.

Spectra averaged over depth for the four analysis locations that are show end-member compositions from Jake_M. Left panel: UV range; Right panel: Part of the VNIR range showing the K and Na lines.

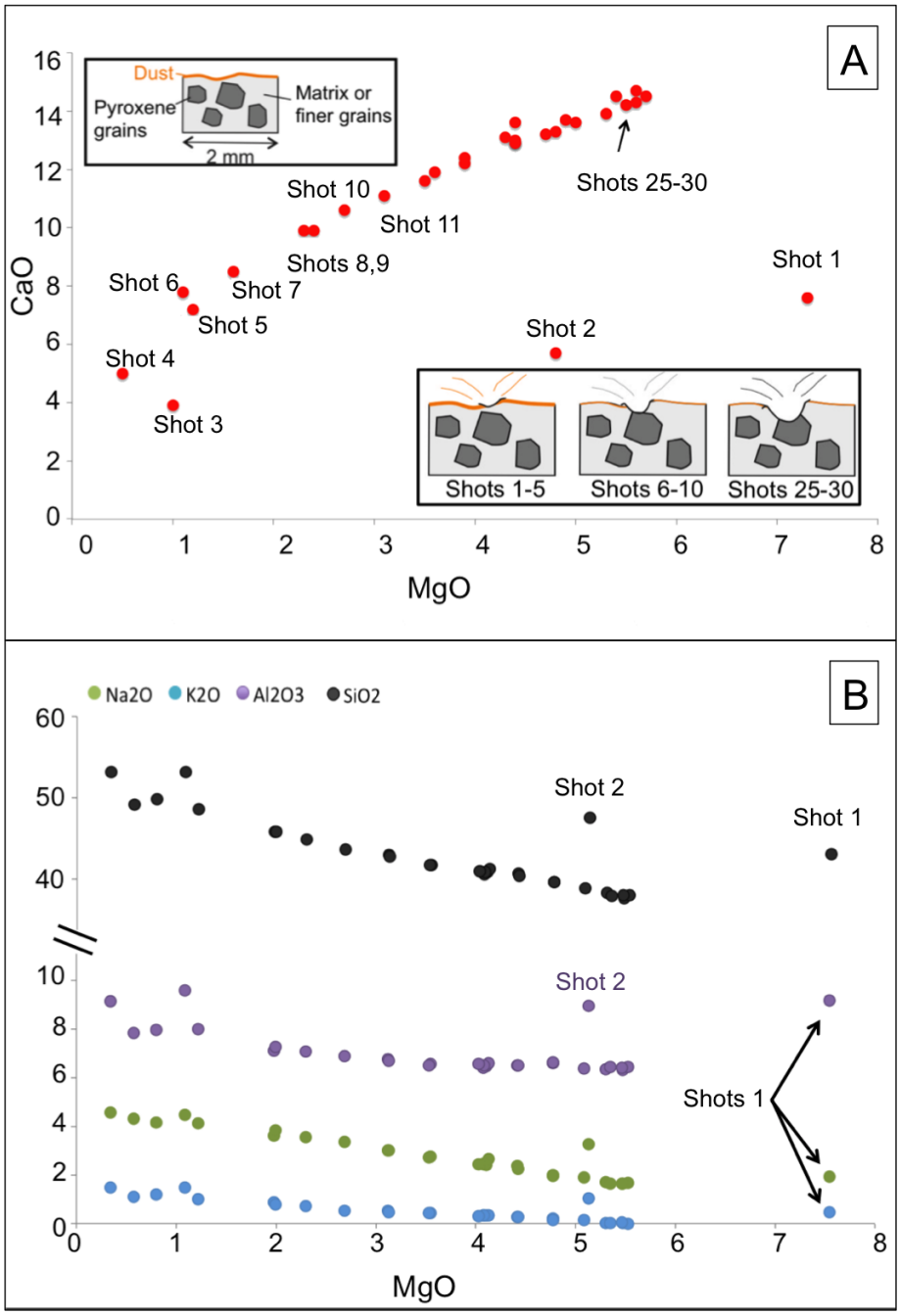

Fig. S4.

(A) CaO *vs*. MgO determined by PLS for ChemCam location 14 on Jake_M. The first two shots show the effect of surface dust; shots 3–30 suggest a mixture dominated by plagioclase and a high-Ca pyroxene with the proportion of pyroxene increasing with depth. (B) SiO_2, Al_2O_3, K_2O, and Na_2O *vs*. MgO in wt. % determined by PLS for ChemCam location 14 on Jake_M. The first two shots show the effect of surface dust. All these elements are decreasing while Mg increases, which is consistent with an interpretation of a Ca-rich pyroxene at depth.

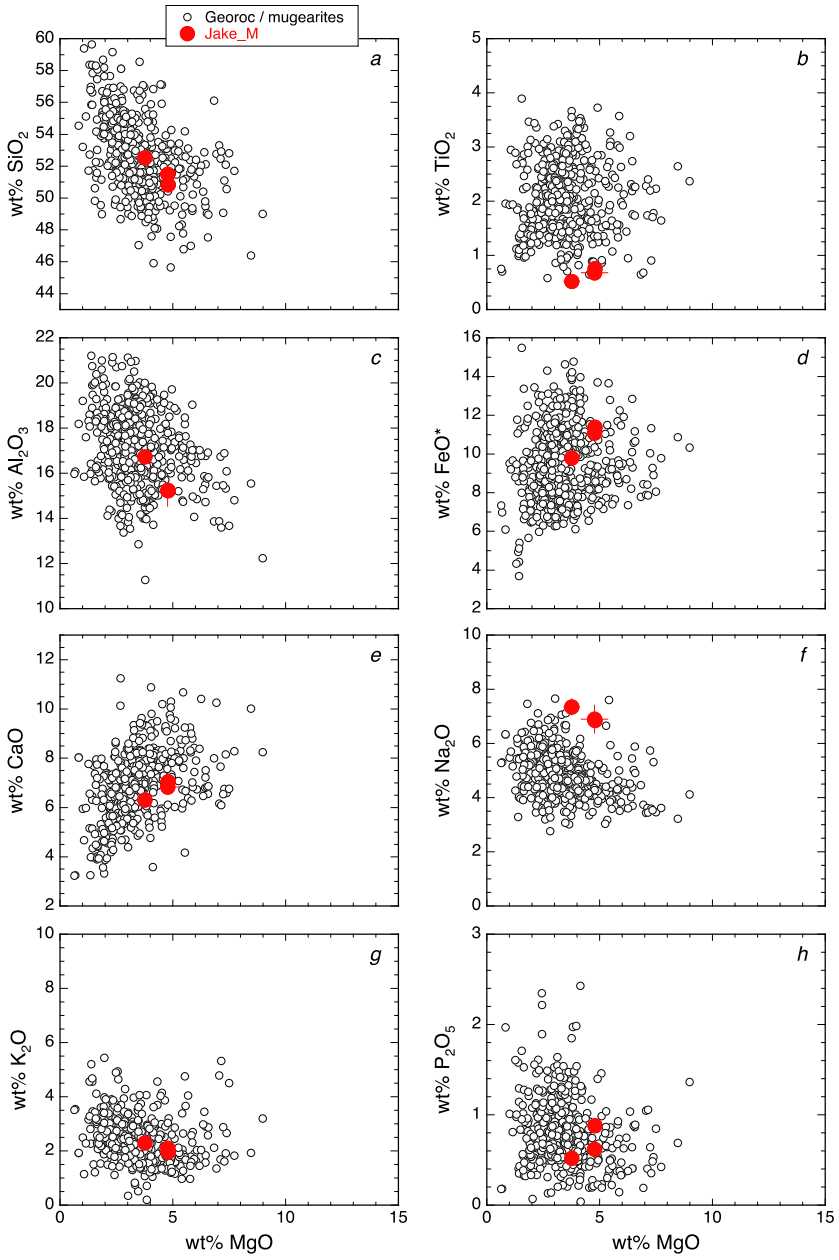

Fig. S5.
Comparison of the three Jake_M analyses (Table 1) to terrestrial rocks labeled mugearites in the Georoc database (*25*); all analyses normalized to 100% on a H_2O-, CO_2-, S-, and Cl-free basis. (a) SiO_2-MgO, (b) TiO_2-MgO, (c) Al_2O_3-MgO, (d) FeO*-MgO, (e) CaO-MgO, (f) Na_2O-MgO, (g) K_2O-MgO, (h) P_2O_5-MgO; FeO* = all Fe as FeO.

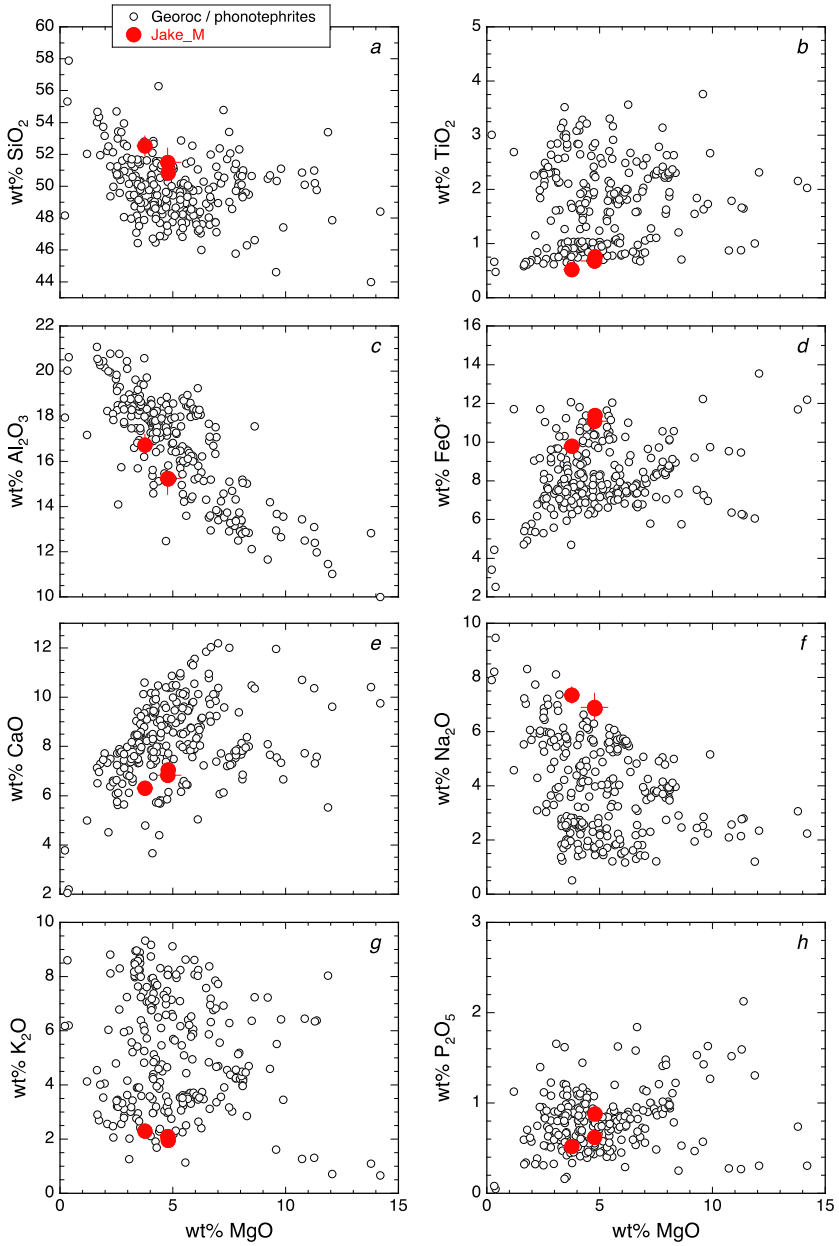

Fig. S6.
Comparison of the three Jake_M analyses (Table 1) to terrestrial rocks labeled phonotephrites in the Georoc database (*25*); all analyses normalized to 100% on a H_2O-, CO_2-, S-, and Cl-free basis. (a) SiO_2-MgO, (b) TiO_2-MgO, (c) Al_2O_3-MgO, (d) FeO*-MgO, (e) CaO-MgO, (f) Na_2O-MgO, (g) K_2O-MgO, (h) P_2O_5-MgO; FeO* = all Fe as FeO.

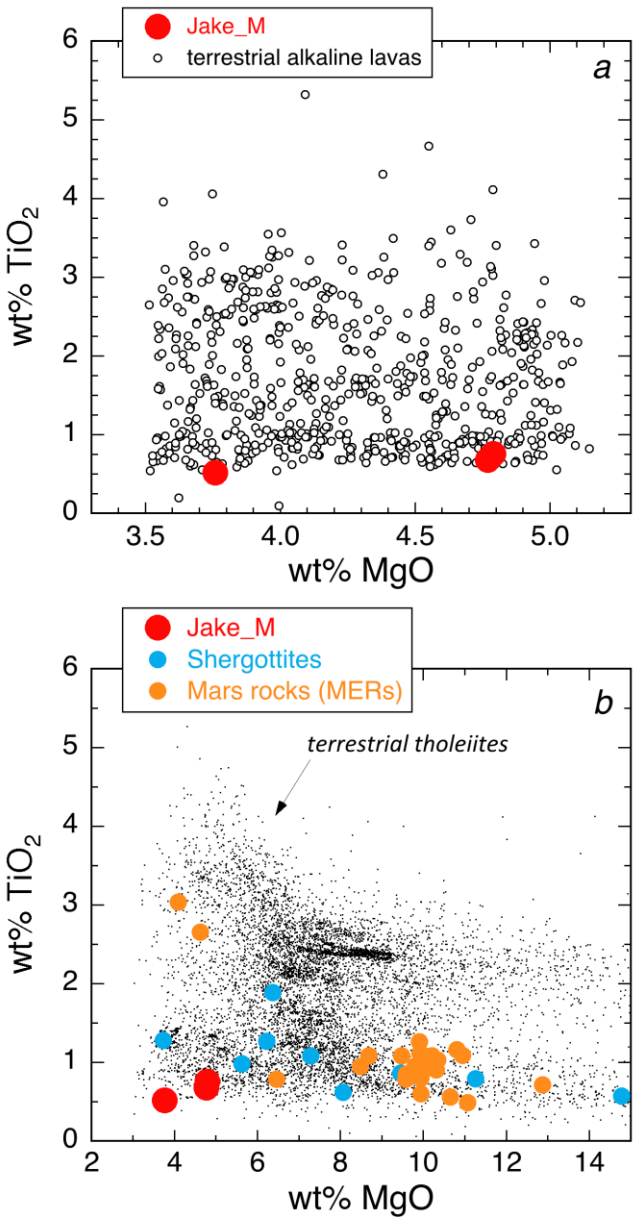

Fig. S7.
(a) TiO_2 *vs*. MgO comparison between terrestrial alkaline rocks (*25*) [those lying above the alkaline-subalkaline boundary (*23*) in Na_2O+K_2O *vs*. SiO_2 space] with 50–55 wt. % SiO_2 and 3.5–5 wt. % MgO and Jake_M (Table 1). (b) TiO_2 *vs*. MgO comparison between terrestrial tholeiitic rocks (i.e., compositions that plot below the alkaline-subalkaline boundary) with 47–53 wt. % SiO_2 and 3–15 wt. % MgO (*25*) and Jake_M (Table 1), shergottites (*9*), and martian rocks analyzed by the Mars Exploration Rovers (*10, 75-77*). The two high TiO_2 martian rocks are Wishstone and Champagne (*10*). All analyses in (a) and (b) have been normalized to 100 wt. % on a volatile-free basis with all Fe as FeO; terrestrial lavas were culled from the Georoc database (*25*) prior to normalization.

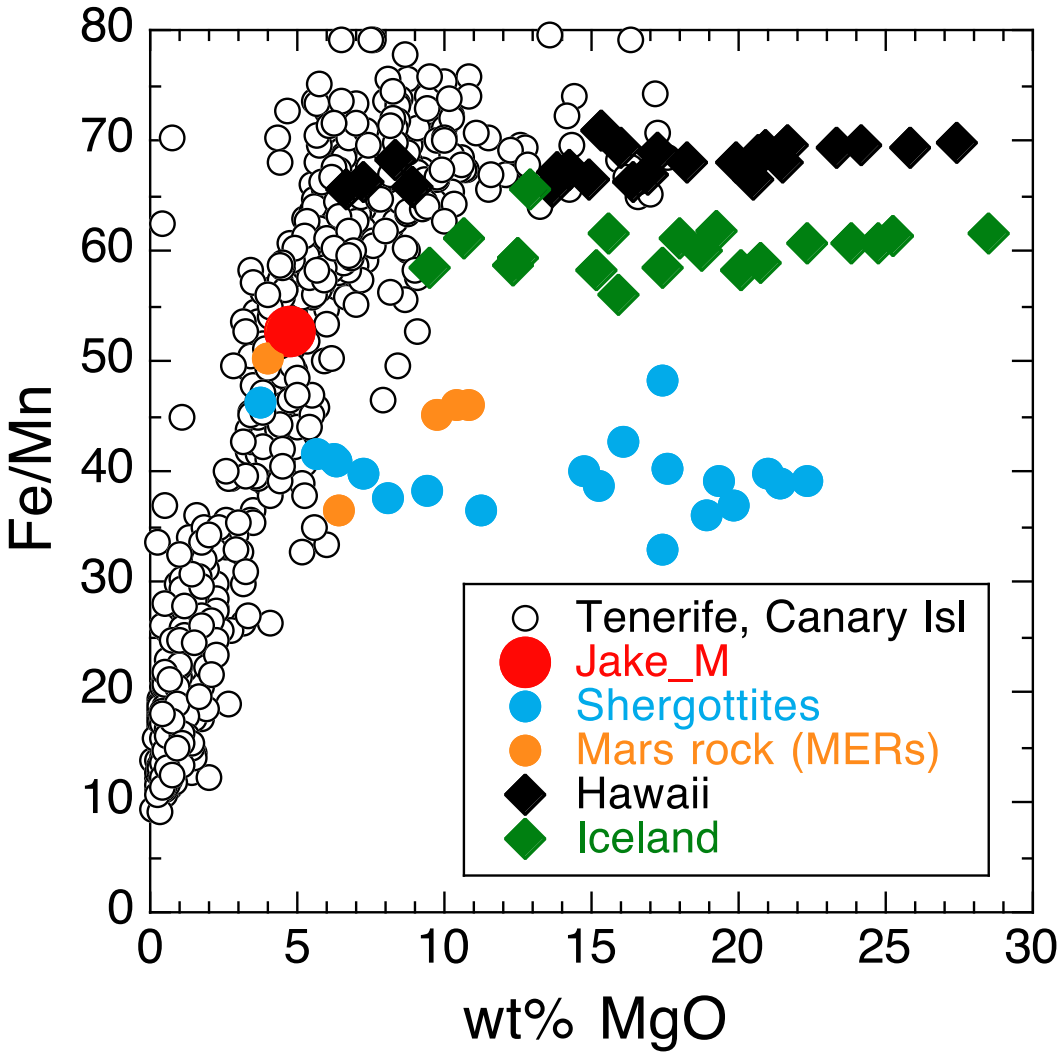

Fig. S8.
Fe/Mn (by weight) *vs*. MgO for Tenerife lavas (*25*), Jake_M (JM2n, Table 1), shergottites (*9*, *73*), "abraded" Mars surface rock compositions analyzed by the Mars Exploration Rovers (*10*, *76*) and high-precision Fe/Mn measurements on Hawaiian and Icelandic basalts (*93*, *94*). The 13 Tenerife lavas with Fe/Mn > 80 are not plotted and most likely represent analytical errors (high Fe/Mn correlates with low, i.e., ≤0.1 wt. %, MnO values). One-sigma errors for the Hawaiian and Icelandic lavas are smaller than the size of the symbols.

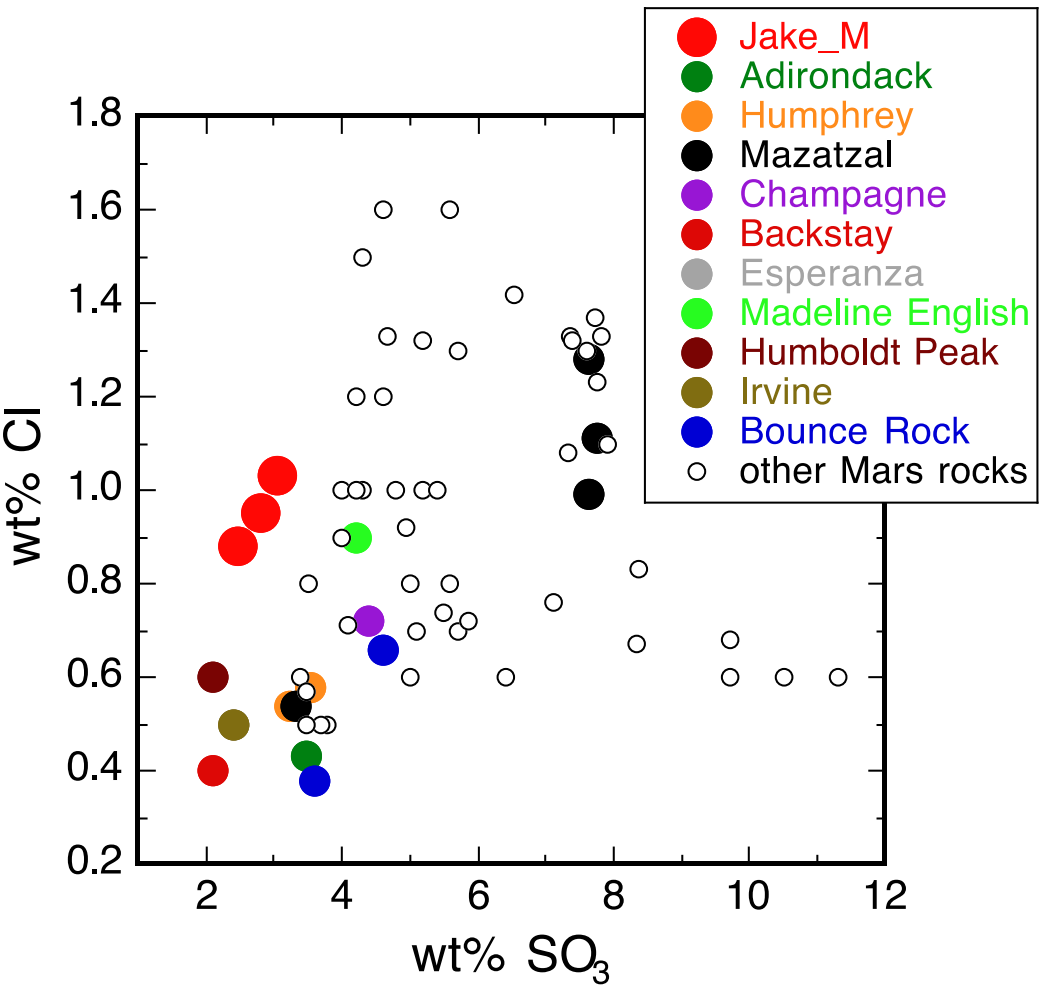

Fig. S9.
SO_3 *vs*. Cl (both in wt. %) in unbrushed and unabraded (i.e., "as is") rocks analyzed by the MERs (*10, 75, 76*) and in Jake_M (Table 1); note that Esperanza plots beneath Irvine.

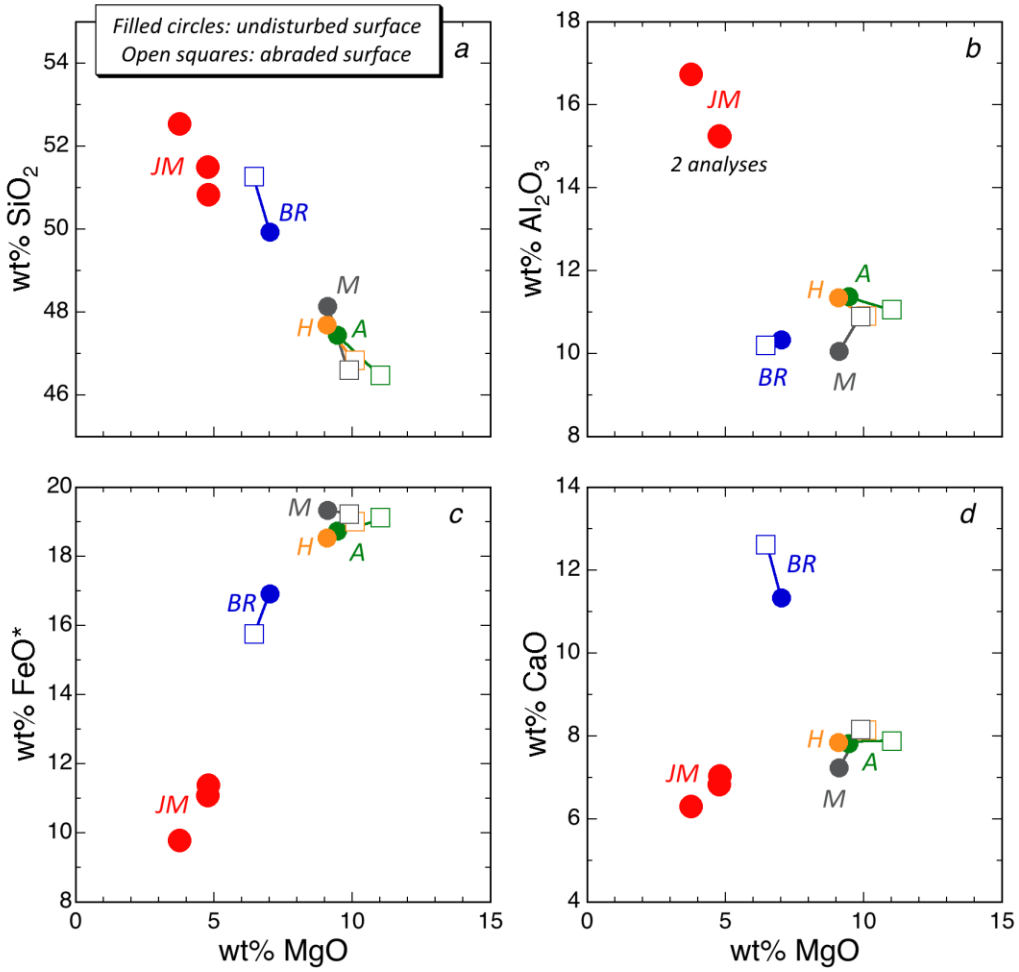

Fig. S10.
Oxide-MgO (all in wt. %) in JM (large filled circles; Table 1) and in unbrushed and unabraded, i.e., "as is" rock analyses (smaller filled circles) and physically abraded rock analyses (open squares) by the MERs (*10, 76*). All analyses have been normalized to 100 wt. % on a SO_3- and Cl-free basis; tie lines connect "as is" and abraded analyses of the same rock/outcrop. Abbreviations: JM = Jake_M; BR = Bounce Rock; M = Mazatzal; H = Humphrey; A = Adirondack. In the case of Mazatzal and Humphrey, multiple analyses have been averaged after being normalized. (a) SiO_2-MgO; (b) Al_2O_3-MgO; (c) FeO*-MgO, where FeO* = all Fe as FeO; (d) CaO-MgO.

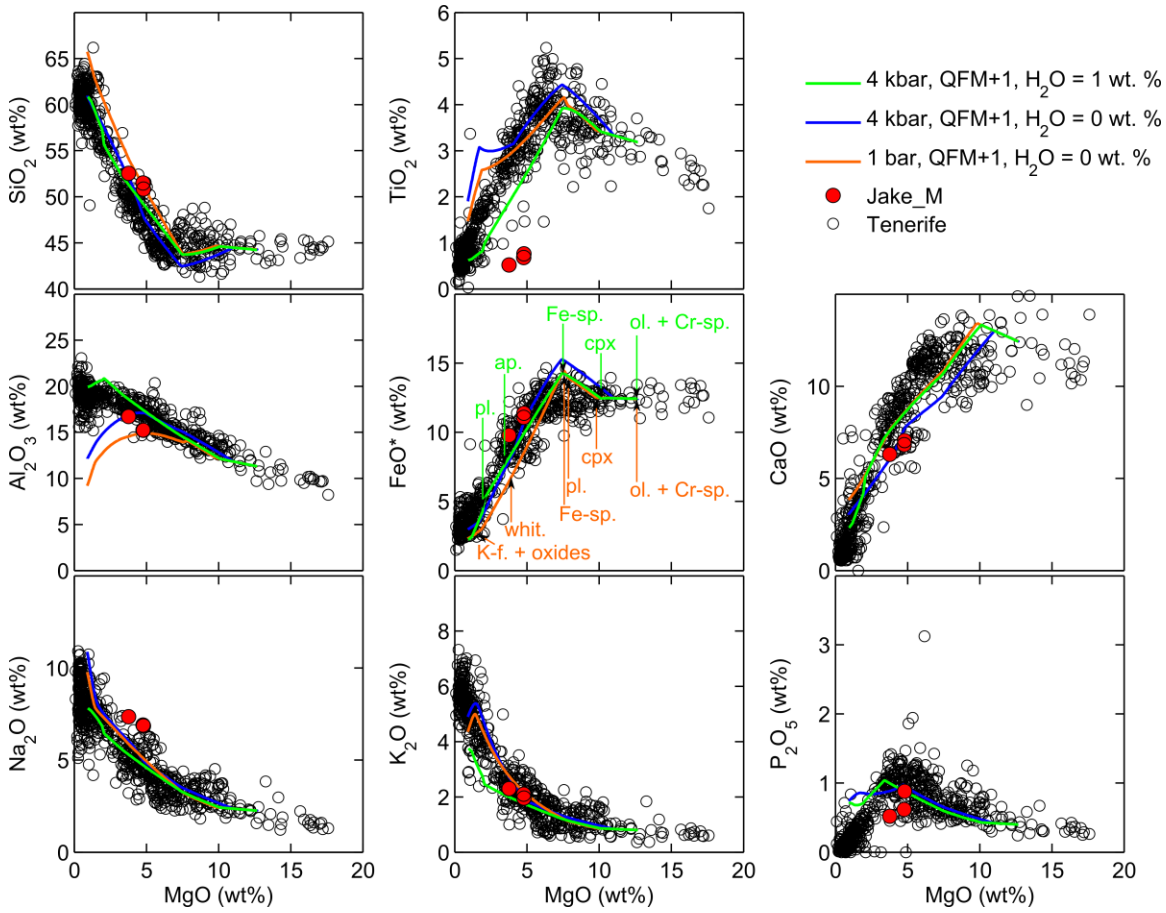

Fig. S11.
Oxide-MgO variation diagrams showing the compositions of Tenerife lavas (*25*), Jake_M (Table 1), and the results of selected MELTS fractional crystallization calculations. The best-fit MELTS calculation (4 kbar, QFM+1, H_2O = 1 wt. %) is plotted in green (Fig. S12 shows how the mismatch between a given MELTS calculation and the Tenerife lavas varies as a function of pressure and initial water content). For comparison, the calculation at 4 kbar, QFM+1 and 0 wt. % water is shown in blue and the calculation at 1 bar, QFM+1 and 0 wt. % water is shown in orange. Colored arrows indicate the entry of phases in the calculated fractional crystallization sequence: ol. = olivine; cpx = clinopyroxene; pl. = plagioclase; Fe-sp. = Fe-rich spinel; K-f. = K-feldspar; whit. = whitlockite; ap. = apatite; oxides = ilmenite.

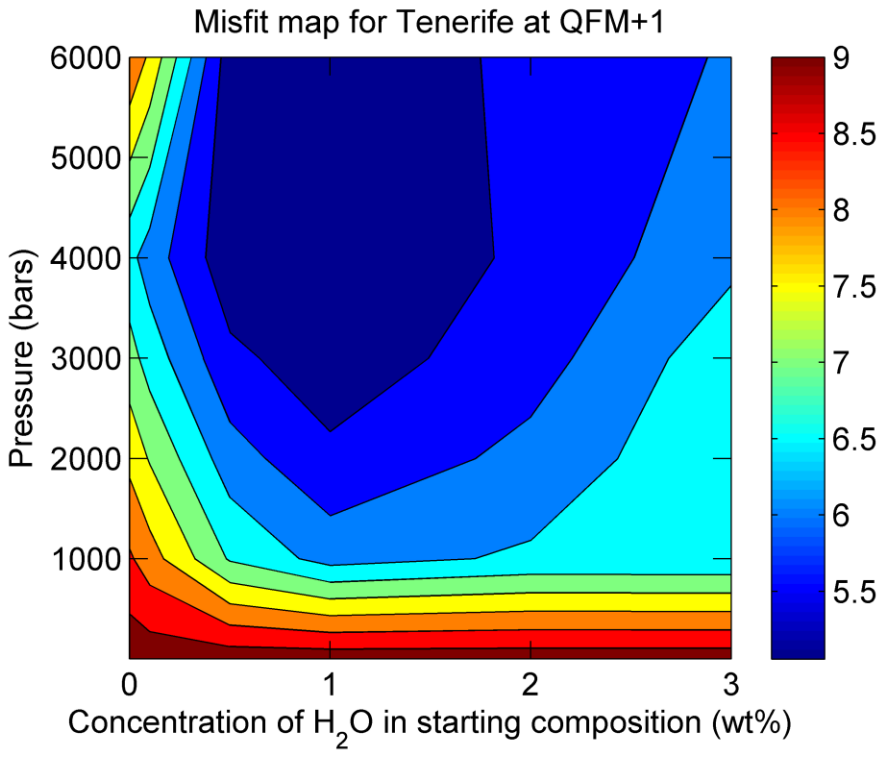

Fig. S12.
Contour plot of misfit between Tenerife data and MELTS fractional crystallization calculations. Calculations performed at QFM+1, at pressures of 1, 1000, 2000, 3000, 4000 and 6000 bars, and water concentrations of 0, 0.1, 0.5, 1, 2 and 3 wt. %. For each of the 36 MELTS calculations, the misfit was calculated by summing the absolute values of the differences between the MELTS curves in SiO_2-, Al_2O_3-, FeO*-, and CaO-MgO space and Tenerife lava compositions with MgO contents between 1 and 12.685 wt. %. The sum of the differences was then divided by the number of Tenerife data points (445) within this MgO concentration range. Note that this misfit parameter does not directly compare with the ones that follow (in Figs. S14, S16, S18, S20, S22, and S24), which are calculated against the three measured Jake_M compositions rather than the whole Tenerife suite. Colored vertical scale bar indicates the degree of misfit; red = large (i.e., worse fit to the Tenerife data) and blue = small (i.e., better fit to the Tenerife data).

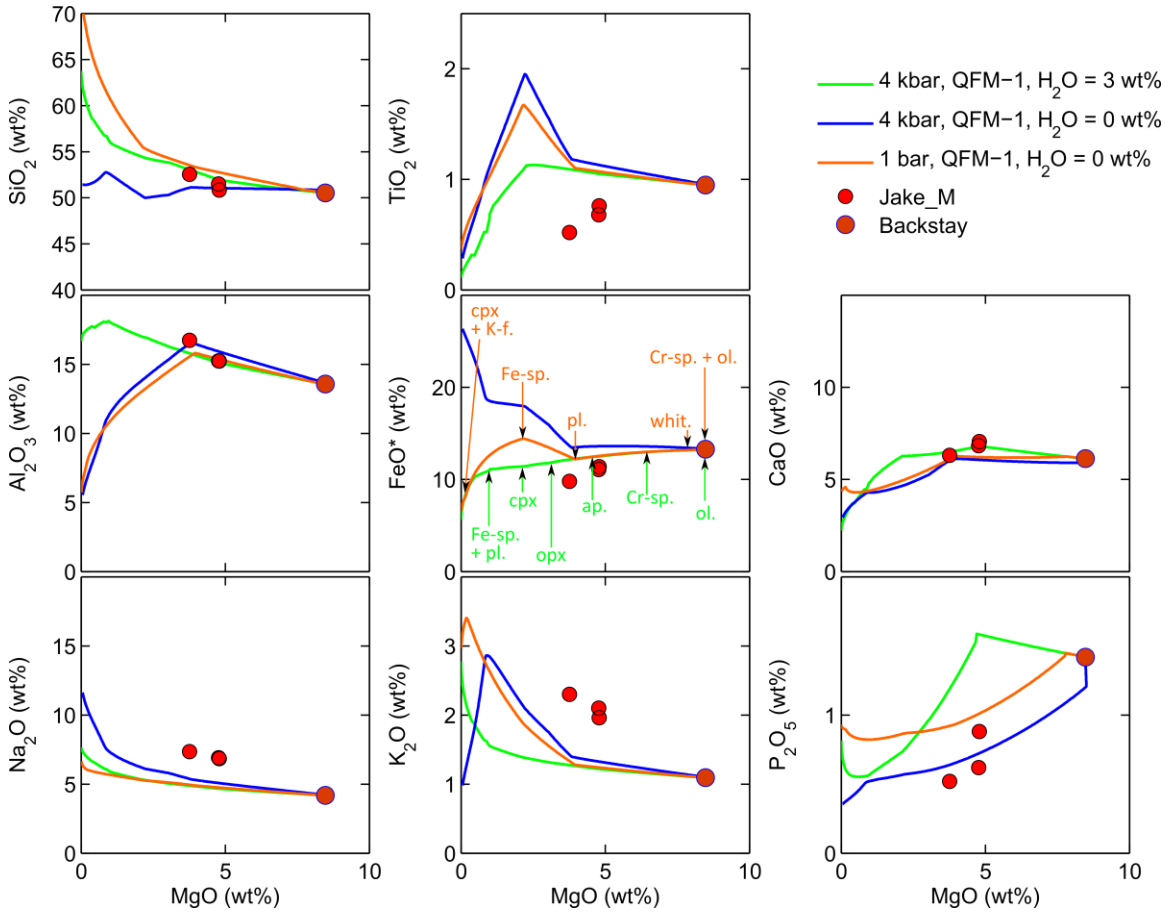

Fig. S13.
MgO variation diagrams for Backstay, Jake_M, and MELTS fractional crystallization calculations at QFM−1. The best-fit calculation (4 kbar and 3 wt. % water) is plotted in green. For comparison, the calculation at 4 kbar and 0 wt. % water is shown in blue, and the calculation at 1 bar and 0 wt. % water is shown in orange. Colored arrows indicate the entry of phases in the calculated fractional crystallization sequence: ol. = olivine; Cr-sp. = Cr-spinel; whit. = whitlockite; ap. = apatite; pl. = plagioclase; opx = orthopyroxene; cpx = clinopyroxene; Fe-sp. = Fe-rich spinel; K-f. = K-feldspar.

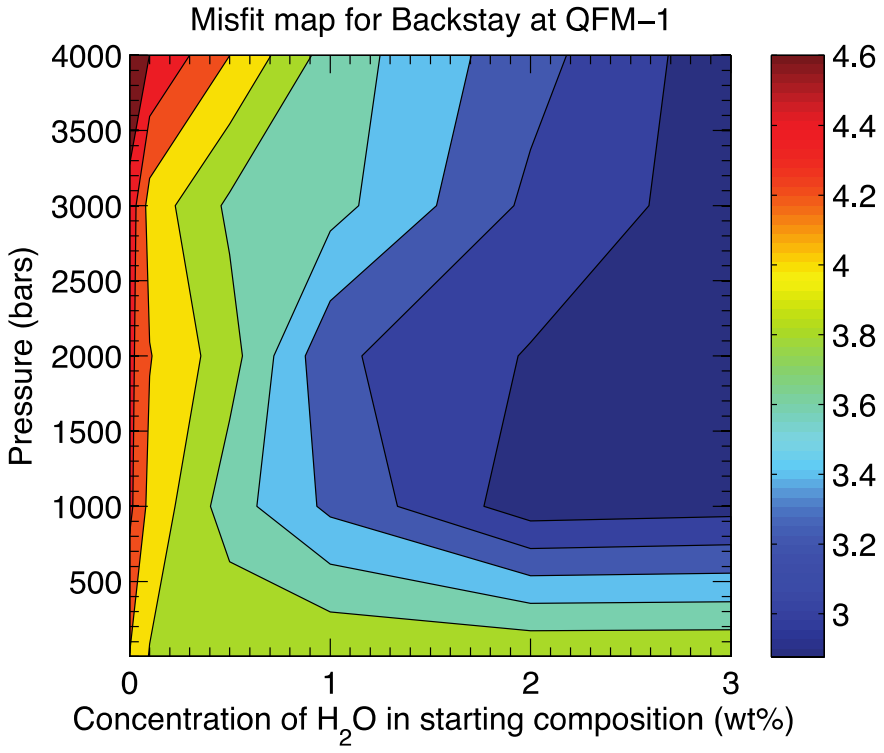

Fig. S14.
Contour plot of misfit between Jake_M and MELTS fractional crystallization calculations at QFM–1 using Backstay as the starting composition. Calculations performed at pressures of 1, 1000, 2000, 3000 and 4000 bars, and water concentrations of 0, 0.1, 0.5, 1, 2 and 3 wt. %. For each of the 30 MELTS calculations, the misfit was calculated by summing the differences between the MELTS curves in SiO_2-, Al_2O_3-, FeO*-, and CaO-MgO space and the three measured Jake_M compositions. The sum of the differences was then divided by three. Note that the misfit in this figure and subsequent figures is not directly comparable to the misfit plotted in Fig. S12, which is calculated against the whole Tenerife suite rather than Jake_M. Colored vertical scale bar indicates the degree of misfit; red = large (i.e., worse fit to Jake_M) and blue = small (i.e., better fit to Jake_M).

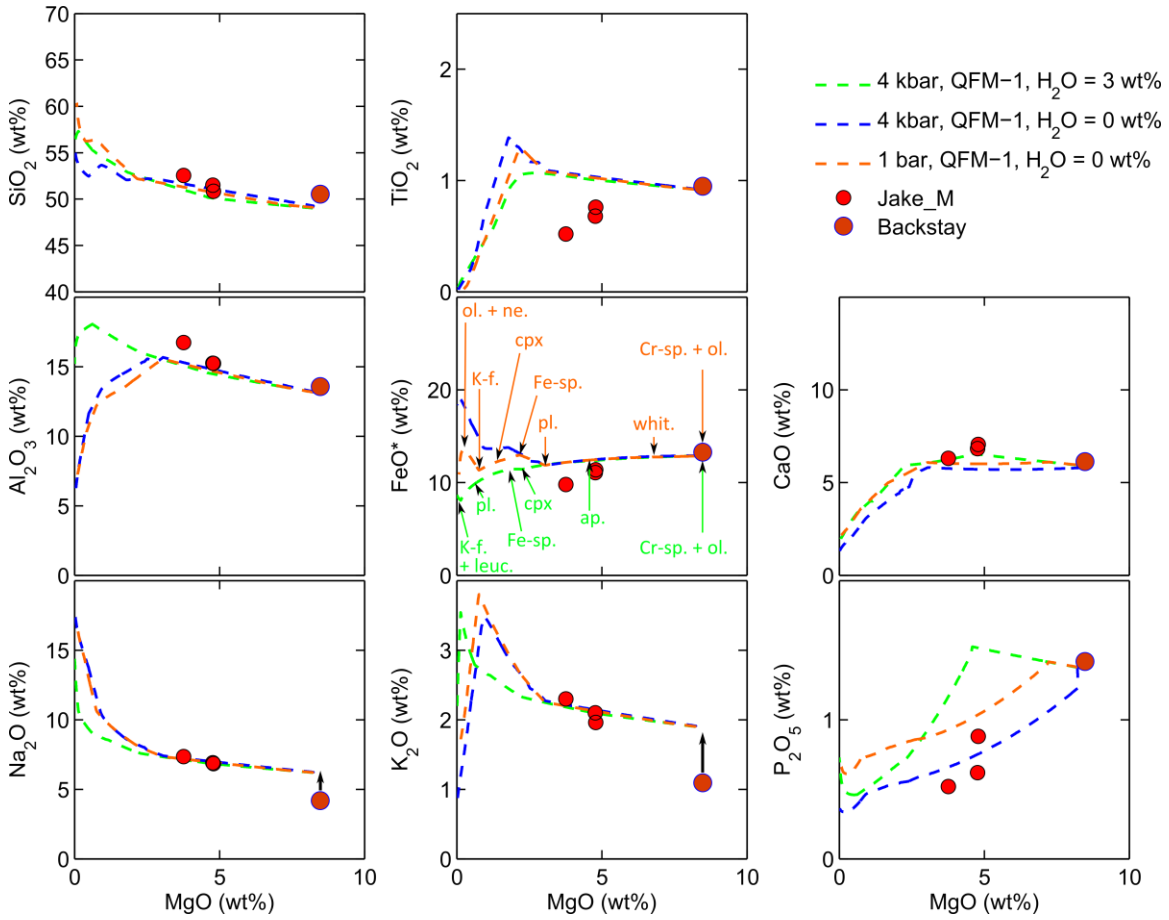

Fig. S15.
MgO variation diagrams for Backstay (with added Na_2O and K_2O so as to match the alkali content of Jake_M), Jake_M, and MELTS fractional crystallization calculations at QFM–1. The best-fit calculation (4 kbar and 3 wt. % water) is plotted in green (note that for the modified and unmodified Backstay composition, the best-fit models occur at the extremes of our investigated pressures and water contents and thus may not represent true minima in pressure-H_2O space). For comparison, the calculation at 4 kbar and 0 wt. % water is shown in blue, and the calculation at 1 bar and 0 wt. % water is shown in orange. Colored arrows indicate the entry of phases in the calculated fractional crystallization sequence: ol. = olivine; Cr-sp. = Cr-spinel; whit. = whitlockite; ap. = apatite; Fe-sp. = Fe-rich spinel; cpx = clinopyroxene; K-f. = K-feldspar; leuc. = leucite. Note that renormalization to 100 wt. % following the addition of alkalis to the Backstay starting composition causes a small decrease in the concentrations of all of the other elements, such that the starting point for the MELTS fractional crystallization calculations is offset from Backstay in all panels. Black arrows in the Na_2O and K_2O variation diagrams emphasize the amount by which Backstay has been enriched in alkalis to create this new starting composition.

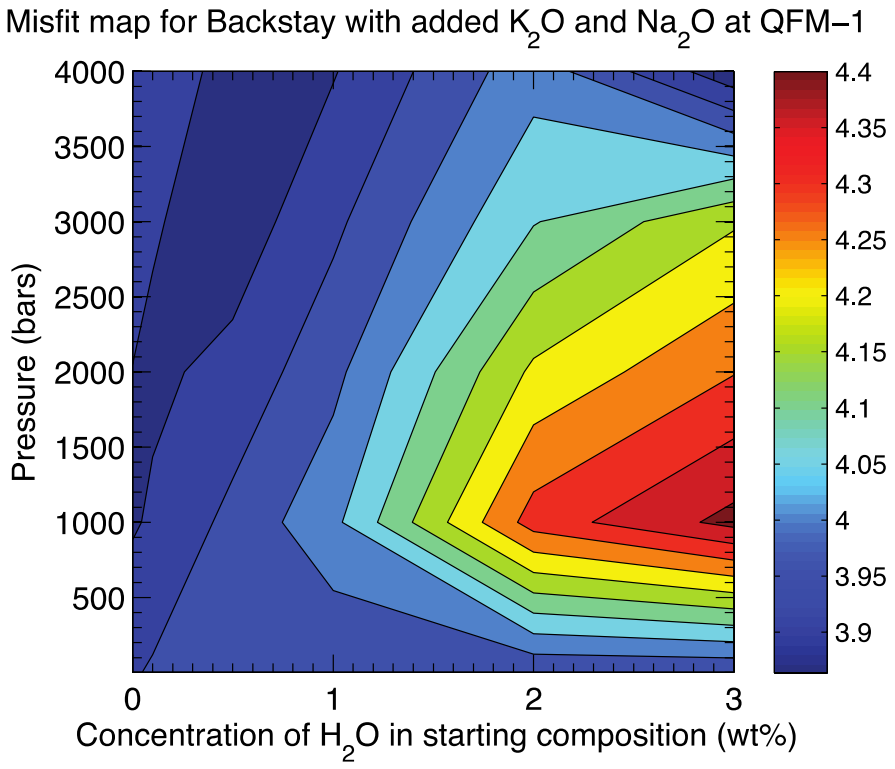

Fig. S16.
Contour plot of misfit between MELTS fractional crystallization calculations at QFM–1, starting with a Backstay composition with added Na_2O and K_2O. Calculations performed at pressures of 1, 1000, 2000, 3000 and 4000 bars, and water concentrations of 0, 0.1, 0.5, 1, 2 and 3 wt. %. For each of the 30 MELTS calculations, the misfit was calculated by summing the differences between the MELTS curves in SiO_2-, Al_2O_3-, FeO*-, and CaO-MgO space and the three measured Jake_M compositions. The sum of the differences was then divided by three. Note that the misfit in this figure and subsequent figures is not directly comparable to the misfit plotted in Fig. S12, which is calculated against the whole Tenerife suite rather than Jake_M. Colored vertical scale bar indicates the degree of misfit; red = large (i.e., worse fit to Jake_M) and blue = small (i.e., better fit to Jake_M).

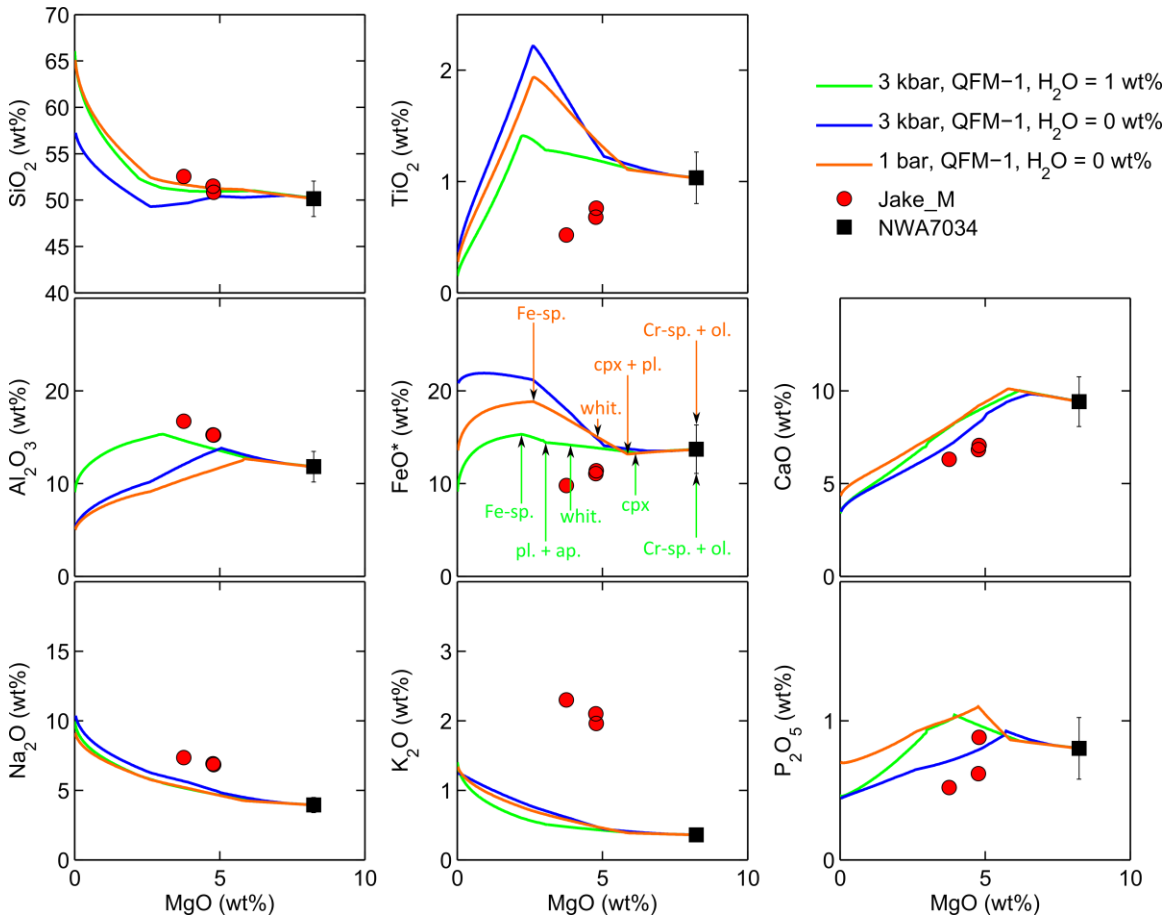

Fig. S17.
MgO variation diagrams for NWA 7034, Jake_M, and MELTS fractional crystallization calculations at QFM−1. The best-fit calculation (3 kbar and 1 wt. % water) is plotted in green. For comparison, the calculation at 3 kbar and 0 wt. % water is shown in blue, and the calculation at 1 bar and 0 wt. % water is shown in orange. Colored arrows indicate the entry of phases in the calculated fractional crystallization sequence: ol. = olivine; Cr-sp. = Cr-spinel; cpx = clinopyroxene; pl. = plagioclase; whit. = whitlockite; ap. = apatite; Fe-sp. = Fe-rich spinel. Error bars on the composition of NWA 7034 are one standard deviation of 225 microprobe analyses of plumose groundmass (*74*).

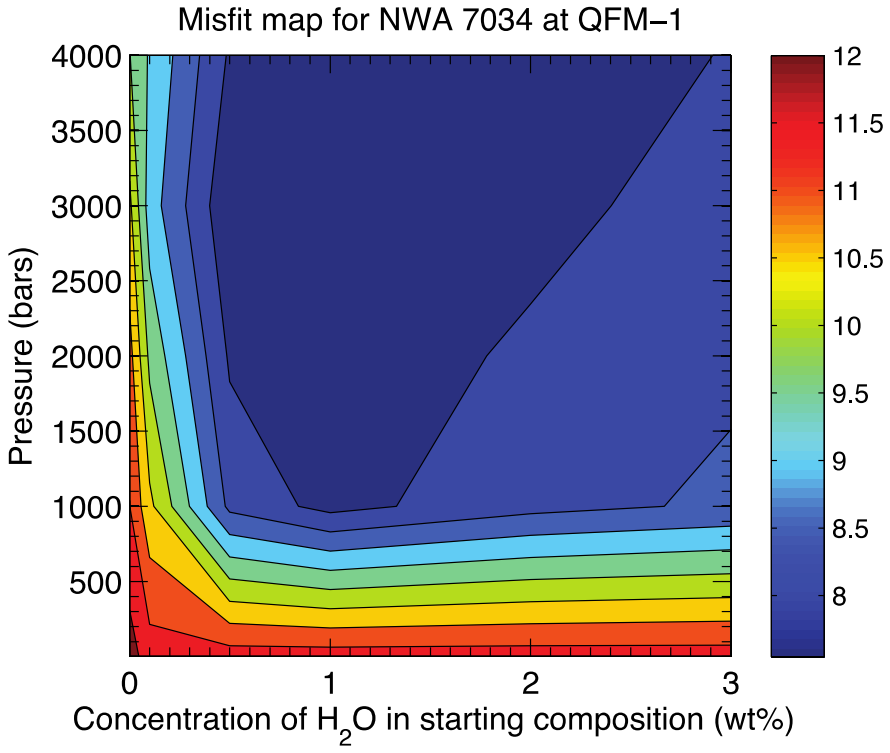

Fig. S18.
Contour plot of misfit between Jake_M and MELTS fractional crystallization calculations at QFM–1 using NWA 7034 as the starting composition. Calculations performed at pressures of 1, 1000, 2000, 3000 and 4000 bars, and water concentrations of 0, 0.1, 0.5, 1, 2 and 3 wt. %. For each of the 30 MELTS calculations, the misfit was calculated by summing the differences between the MELTS curves in SiO_2-, Al_2O_3-, FeO*-, and CaO-MgO space and the three measured Jake_M compositions. The sum of the differences was then divided by three. Note that the misfit in this figure and subsequent figures is not directly comparable to the misfit plotted in Fig. S12, which is calculated against the whole Tenerife suite rather than Jake_M. Colored vertical scale bar indicates the degree of misfit; red = large (i.e., worse fit to Jake_M) and blue = small (i.e., better fit to Jake_M).

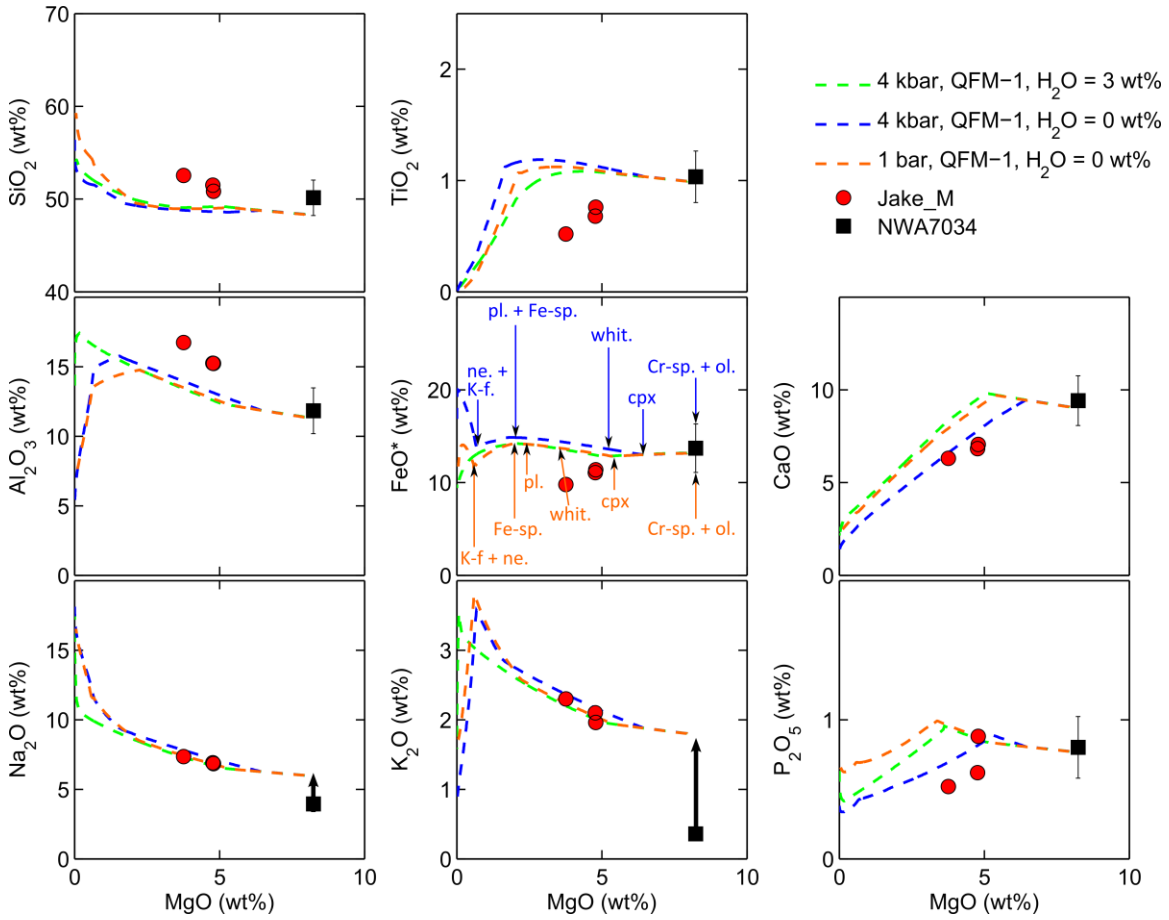

Fig. S19.
MgO variation diagrams for NWA 7034 (with added Na_2O and K_2O so as to match the alkali content of Jake_M), Jake_M, and MELTS fractional crystallization calculations at QFM–1. The best-fit calculation (4 kbar and 0 wt. % water) is plotted in blue and represents the minimum with respect to the investigated region of pressure-H_2O space. For comparison, the calculation at 4 kbar and 3 wt. % water is shown in green, and the calculation at 1 bar and 0 wt. % water is shown in orange. Colored arrows indicate the entry of phases in the calculated fractional crystallization sequence: ol. = olivine; Cr-sp. = Cr-spinel; cpx = clinopyroxene; whit. = whitlockite; pl. = plagioclase; ap. = apatite; Fe-sp. = Fe-rich spinel; K-f. = K-feldspar; ne. = nepheline. Note that renormalization to 100 wt. % following the addition of alkalis to the NWA 7034 starting composition causes a small decrease in the concentrations of all of the other elements, such that the starting point for the MELTS fractional crystallization calculations is offset from NWA 7034 in all panels. Black arrows in the Na_2O and K_2O variation diagrams emphasize the amount by which NWA 7034 has been enriched in alkalis to create this new starting composition. Error bars on the composition of NWA 7034 are one standard deviation of 225 microprobe analyses of plumose groundmass (*74*).

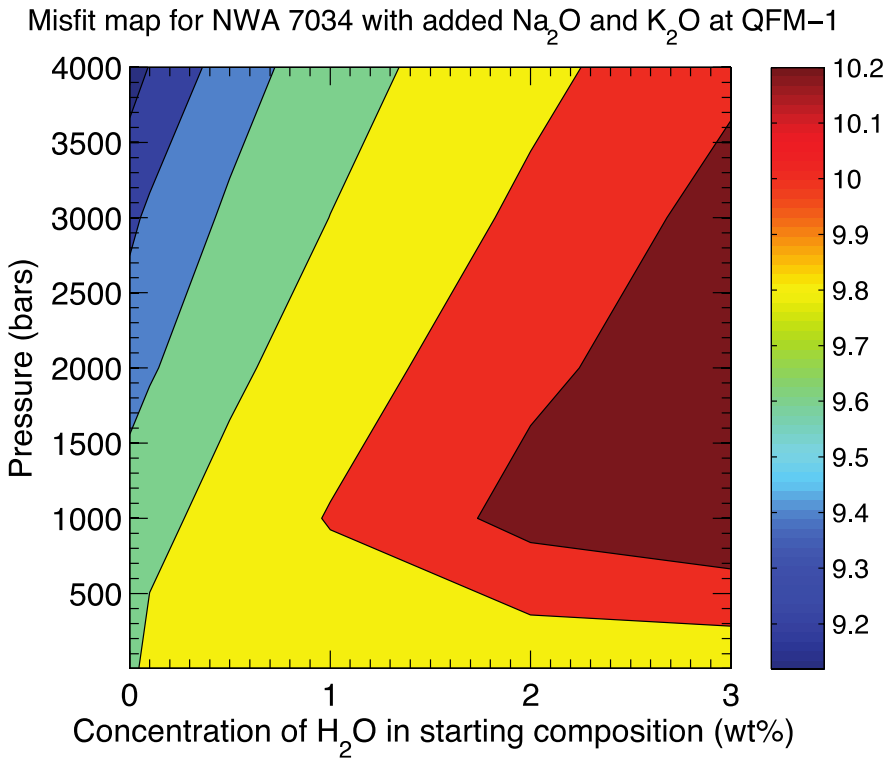

Fig. S20.
Contour plot of misfit between Jake_M and MELTS fractional crystallization calculations at QFM–1 using NWA 7034 with added Na_2O and K_2O as the starting composition. Calculations performed at pressures of 1, 1000, 2000, 3000 and 4000 bars, and water concentrations of 0, 0.1, 0.5, 1, 2 and 3 wt. %. For each of the 30 MELTS calculations, the misfit was calculated by summing the differences between the MELTS curves in SiO_2-, Al_2O_3-, FeO*-, and CaO-MgO space and the three measured Jake_M compositions. The sum of the differences was then divided by three. Note that the misfit in this figure and subsequent figures is not directly comparable to the misfit plotted in Fig. S12, which is calculated against the whole Tenerife suite rather than Jake_M. Colored vertical scale bar indicates the degree of misfit; red = large (i.e., worse fit to Jake_M) and blue = small (i.e., better fit to Jake_M).

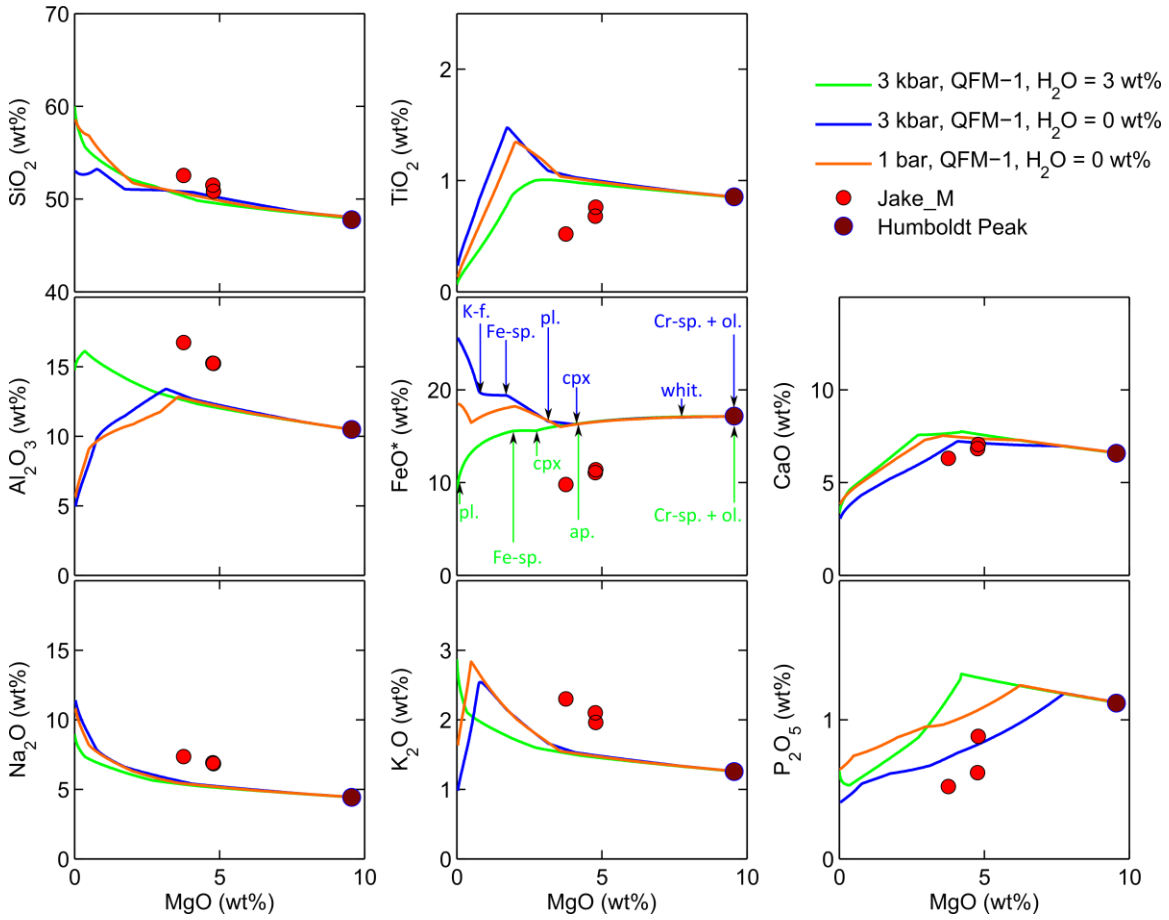

Fig. S21.
MgO variation diagrams for Humboldt Peak, Jake_M, and MELTS fractional crystallization calculations at QFM−1. The best-fit calculation (3 kbar and 0 wt. % water) is plotted in blue. For comparison, the calculation at 3 kbar and 3 wt. % water is shown in green, and the calculation at 1 bar and 0 wt. % water is shown in orange. Colored arrows indicate the entry of phases in the calculated fractional crystallization sequence ol. = olivine; Cr-sp. = Cr-spinel; whit. = whitlockite; ap. = apatite; pl. = plagioclase; cpx = clinopyroxene; Fe-sp. = Fe-rich spinel; K-f. = K-feldspar.

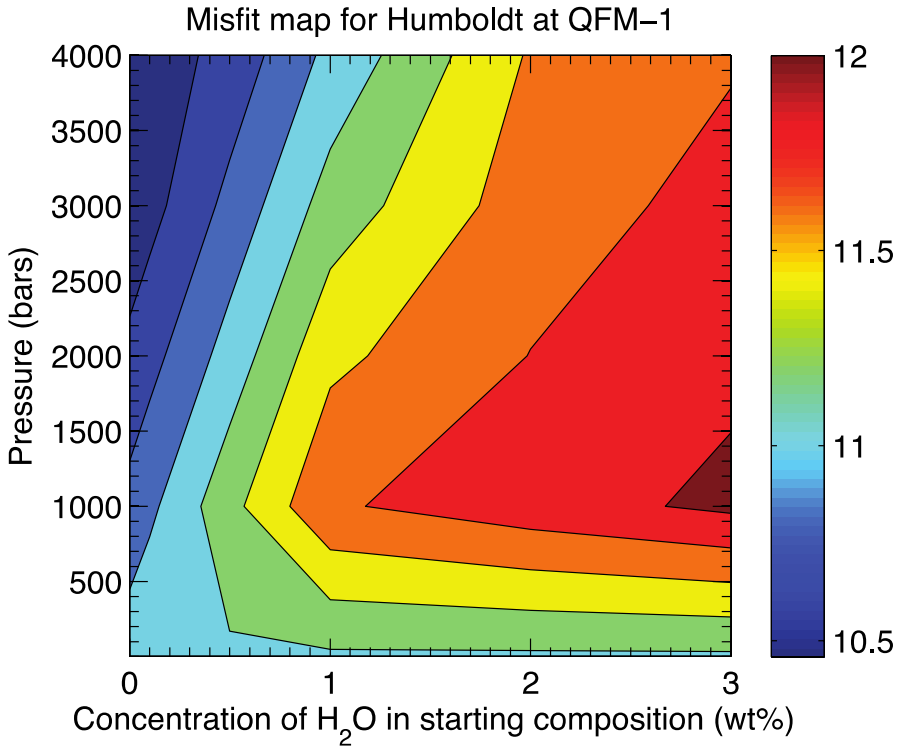

Fig. S22.
Contour plot of misfit between Jake_M and MELTS fractional crystallization calculations at QFM–1 using Humboldt Peak as the starting composition. Calculations performed at pressures of 1, 1000, 2000, 3000 and 4000 bars, and water concentrations of 0, 0.1, 0.5, 1, 2 and 3 wt. %. For each of the 30 MELTS calculations, the misfit was calculated by summing the differences between the MELTS curves in SiO_2-, Al_2O_3-, FeO*-, and CaO-MgO space and the three measured Jake_M compositions. The sum of the differences was then divided by three. Note that the misfit in this figure and subsequent figures is not directly comparable to the misfit plotted in Fig. S12, which is calculated against the whole Tenerife suite rather than Jake_M. Colored vertical scale bar indicates the degree of misfit; red = large (i.e., worse fit to Jake_M) and blue = small (i.e., better fit to Jake_M).

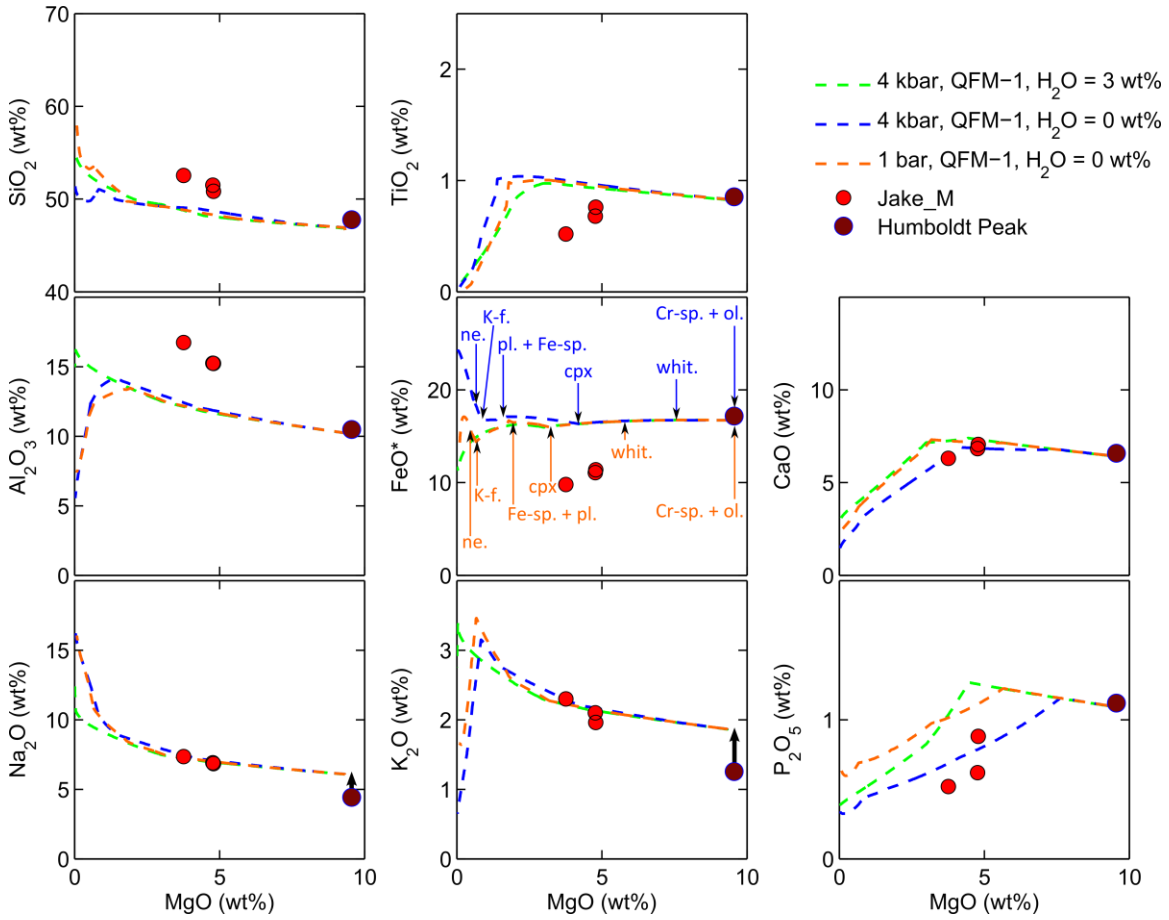

Fig. S23.
MgO variation diagrams for Humboldt Peak (with added Na_2O and K_2O so as to match the alkali content of Jake_M), Jake_M, and MELTS fractional crystallization calculations at QFM–1. The best-fit calculation (4 kbar and 0 wt. % water) is plotted in blue. For comparison, the calculation at 4 kbar and 3 wt. % water is shown in green, and the calculation at 1 bar and 0 wt. % water is shown in orange. Colored arrows indicate the entry of phases in the calculated fractional crystallization sequence: ol. = olivine; Cr-sp. = Cr-spinel; whit. = whitlockite; ap. = apatite; cpx = clinopyroxene; pl. = plagioclase; Fe-sp. = Fe-rich spinel; opx = orthopyroxene; ne. = nepheline; K-f. = K-feldspar. Note that renormalization to 100 wt. % following the addition of alkalis to the Humboldt Peak starting composition causes a small decrease in the concentrations of all of the other elements, such that the starting point for the MELTS fractional crystallization calculations is offset from Humboldt Peak in all panels. Black arrows in the Na_2O and K_2O variation diagrams emphasize the amount by which Humboldt Peak has been enriched in alkalis to create this new starting composition.

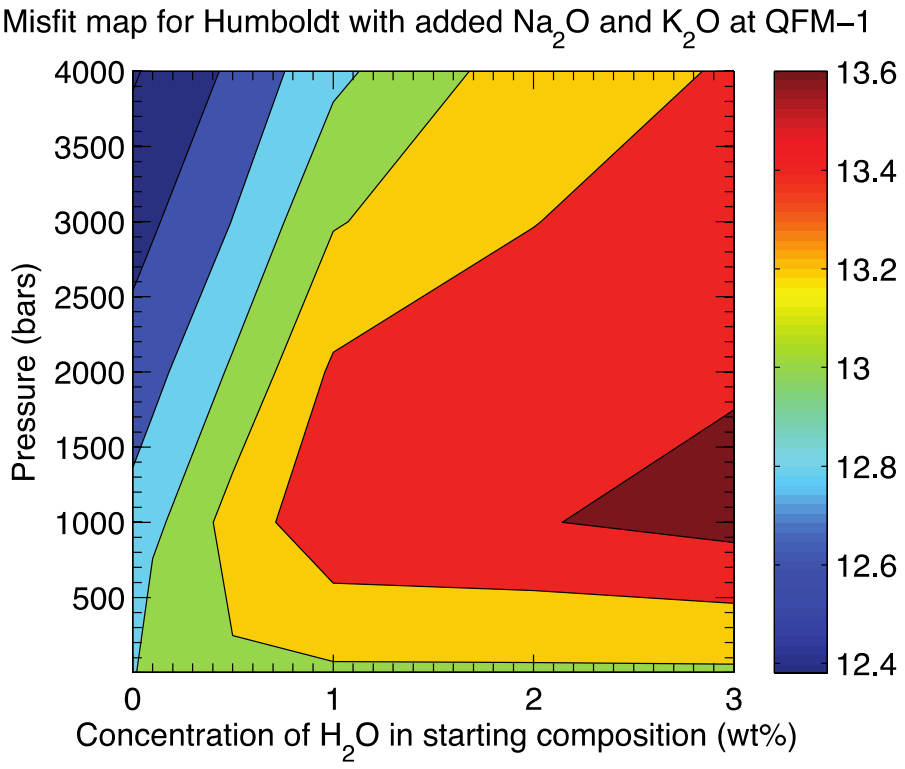

Fig. S24.
Contour plot of misfit between Jake_M and MELTS fractional crystallization calculations at QFM–1 using Humboldt Peak with added Na_2O and K_2O as the starting composition. Calculations performed at pressures of 1, 1000, 2000, 3000 and 4000 bars, and water concentrations of 0, 0.1, 0.5, 1, 2 and 3 wt. %. For each of the 30 MELTS calculations, the misfit was calculated by summing the differences between the MELTS curves in SiO_2-, Al_2O_3-, FeO*-, and CaO-MgO space and the three measured Jake_M compositions. The sum of the differences was then divided by three. Note that the misfit in this figure and subsequent figures is not directly comparable to the misfit plotted in Fig. S12, which is calculated against the whole Tenerife suite rather than Jake_M. Colored vertical scale bar indicates the degree of misfit; red = large (i.e., worse fit to Jake_M) and blue = small (i.e., better fit to Jake_M).

Mars Science Laboratory (MSL) Science Team

Aalto University
Osku Kemppinen

Applied Physics Laboratory (APL) at Johns Hopkins University
Nathan Bridges, Jeffrey R. Johnson, Michelle Minitti

Applied Research Associates, Inc. (ARA)
David Cremers

Arizona State University (ASU)
James F. Bell III, Lauren Edgar, Jack Farmer, Austin Godber, Meenakshi Wadhwa, Danika Wellington

Ashima Research
Ian McEwan, Claire Newman, Mark Richardson

ATOS Origin
Antoine Charpentier, Laurent Peret

Australian National University (ANU)
Penelope King

Bay Area Environmental Research Institute (BAER)
Jennifer Blank

Big Head Endian LLC
Gerald Weigle

Brock University
Mariek Schmidt

Brown University
Shuai Li, Ralph Milliken, Kevin Robertson, Vivian Sun

California Institute of Technology (Caltech)
Michael Baker, Christopher Edwards, Bethany Ehlmann, Kenneth Farley, Jennifer Griffes, John Grotzinger, Hayden Miller, Megan Newcombe, Cedric Pilorget, Melissa Rice, Kirsten Siebach, Katie Stack, Edward Stolper

Canadian Space Agency (CSA)
Claude Brunet, Victoria Hipkin, Richard Léveillé, Geneviève Marchand, Pablo Sobrón Sánchez

Capgemini France
Laurent Favot

Carnegie Institution of Washington
George Cody, Andrew Steele

Carnegie Mellon University
Lorenzo Flückiger, David Lees, Ara Nefian

Catholic University of America
Mildred Martin

Centre National de la Recherche Scientifique (CNRS)
Marc Gailhanou, Frances Westall, Guy Israël

Centre National d'Etudes Spatiales (CNES)
Christophe Agard, Julien Baroukh, Christophe Donny, Alain Gaboriaud, Philippe Guillemot, Vivian Lafaille, Eric Lorigny, Alexis Paillet, René Pérez, Muriel Saccoccio, Charles Yana

Centro de Astrobiología (CAB)

Carlos Armiens-Aparicio, Javier Caride Rodríguez, Isaías Carrasco Blázquez, Felipe Gómez Gómez , Javier Gómez-Elvira, Sebastian Hettrich, Alain Lepinette Malvitte, Mercedes Marín Jiménez, Jesús Martínez-Frías, Javier Martín-Soler, F. Javier Martín-Torres, Antonio Molina Jurado, Luis Mora-Sotomayor, Guillermo Muñoz Caro, Sara Navarro López, Verónica Peinado-González, Jorge Pla-García, José Antonio Rodriguez Manfredi, Julio José Romeral-Planelló, Sara Alejandra Sans Fuentes, Eduardo Sebastian Martinez, Josefina Torres Redondo, Roser Urqui-O'Callaghan, María-Paz Zorzano Mier

Chesapeake Energy
Steve Chipera

Commissariat à l'Énergie Atomique et aux Énergies Alternatives (CEA)
Jean-Luc Lacour, Patrick Mauchien, Jean-Baptiste Sirven

Concordia College
Heidi Manning

Cornell University
Alberto Fairén, Alexander Hayes, Jonathan Joseph, Steven Squyres, Robert Sullivan, Peter Thomas

CS Systemes d'Information
Audrey Dupont

Delaware State University
Angela Lundberg, Noureddine Melikechi, Alissa Mezzacappa

Denver Museum of Nature & Science
Julia DeMarines, David Grinspoon

Deutsches Zentrum für Luft- und Raumfahrt (DLR)
Günther Reitz

eINFORMe Inc. (at NASA GSFC)
Benito Prats

Finnish Meteorological Institute
Evgeny Atlaskin, Maria Genzer, Ari-Matti Harri, Harri Haukka, Henrik Kahanpää, Janne Kauhanen, Osku Kemppinen, Mark Paton, Jouni Polkko, Walter Schmidt, Tero Siili

GeoRessources
Cécile Fabre

Georgia Institute of Technology
James Wray, Mary Beth Wilhelm

Géosciences Environnement Toulouse (GET)
Franck Poitrasson

Global Science & Technology, Inc.
Kiran Patel

Honeybee Robotics
Stephen Gorevan, Stephen Indyk, Gale Paulsen

Imperial College
Sanjeev Gupta

Indiana University Bloomington
David Bish, Juergen Schieber

Institut d'Astrophysique Spatiale (IAS)
Brigitte Gondet, Yves Langevin

Institut de Chimie des Milieux et Matériaux de Poitier (IC2MP)
Claude Geffroy

Institut de Recherche en Astrophysique et Planétologie (IRAP), Université de Toulouse
David Baratoux, Gilles Berger, Alain Cros, Claude d'Uston, Olivier Forni, Olivier Gasnault, Jérémie Lasue, Qiu-Mei Lee, Sylvestre Maurice, Pierre-Yves Meslin, Etienne Pallier, Yann Parot, Patrick Pinet, Susanne Schröder, Mike Toplis

Institut des Sciences de la Terre (ISTerre)
Éric Lewin

inXitu
Will Brunner

Jackson State University
Ezat Heydari

Jacobs Technology
Cherie Achilles, Dorothy Oehler, Brad Sutter

Laboratoire Atmosphères, Milieux, Observations Spatiales (LATMOS)
Michel Cabane, David Coscia, Guy Israël, Cyril Szopa, Samuel Teinturier

Laboratoire de Géologié de Lyon : Terre, Planète, Environnement (LGL-TPE)
Gilles Dromart

Laboratoire de Minéralogie et Cosmochimie du Muséum (LMCM)
François Robert, Violaine Sautter

Laboratoire de Planétologie et Géodynamique de Nantes (LPGN)
Stéphane Le Mouélic, Nicolas Mangold, Marion Nachon

Laboratoire Génie des Procédés et Matériaux (LGPM)
Arnaud Buch

Laboratoire Interuniversitaire des Systèmes Atmosphériques (LISA)
Fabien Stalport, Patrice Coll, Pascaline François, François Raulin

Lightstorm Entertainment Inc.
James Cameron

Los Alamos National Lab (LANL)
Sam Clegg, Agnès Cousin, Dorothea DeLapp, Robert Dingler, Ryan Steele Jackson, Stephen Johnstone, Nina Lanza, Cynthia Little, Tony Nelson, Roger C. Wiens, Richard B. Williams

Lunar and Planetary Institute (LPI)
Laurel Kirkland, Allan Treiman

Malin Space Science Systems (MSSS)
Burt Baker, Bruce Cantor, Michael Caplinger, Scott Davis, Brian Duston, Kenneth Edgett, Donald Fay, Craig Hardgrove, David Harker, Paul Herrera, Elsa Jensen, Megan R. Kennedy, Gillian Krezoski, Daniel Krysak, Leslie Lipkaman, Michael Malin, Elaina McCartney, Sean McNair, Brian Nixon, Liliya Posiolova, Michael Ravine, Andrew Salamon, Lee Saper, Kevin Stoiber, Kimberley Supulver, Jason Van Beek, Tessa Van Beek, Robert Zimdar

Massachusetts Institute of Technology (MIT)
Katherine Louise French, Karl Iagnemma, Kristen Miller, Roger Summons

Max Planck Institute for Solar System Research
Fred Goesmann, Walter Goetz, Stubbe Hviid

Microtel

Micah Johnson, Matthew Lefavor, Eric Lyness

Mount Holyoke College
Elly Breves, M. Darby Dyar, Caleb Fassett

NASA Ames
David F. Blake, Thomas Bristow, David DesMarais, Laurence Edwards, Robert Haberle, Tori Hoehler, Jeff Hollingsworth, Melinda Kahre, Leslie Keely, Christopher McKay, Mary Beth Wilhelm

NASA Goddard Space Flight Center (GSFC)
Lora Bleacher, William Brinckerhoff, David Choi, Pamela Conrad, Jason P. Dworkin, Jennifer Eigenbrode, Melissa Floyd, Caroline Freissinet, James Garvin, Daniel Glavin, Daniel Harpold, Paul Mahaffy, David K. Martin, Amy McAdam, Alexander Pavlov, Eric Raaen, Michael D. Smith, Jennifer Stern, Florence Tan, Melissa Trainer

NASA Headquarters
Michael Meyer, Arik Posner, Mary Voytek

NASA Jet Propulsion Laboratory (JPL)
Robert C, Anderson, Andrew Aubrey, Luther W. Beegle, Alberto Behar, Diana Blaney, David Brinza, Fred Calef, Lance Christensen, Joy Crisp, Lauren DeFlores, Bethany Ehlmann, Jason Feldman, Sabrina Feldman, Gregory Flesch, Joel Hurowitz, Insoo Jun, Didier Keymeulen, Justin Maki, Michael Mischna, John Michael Morookian, Timothy Parker, Betina Pavri, Marcel Schoppers, Aaron Sengstacken, John J. Simmonds, Nicole Spanovich, Manuel de la Torre Juarez, Ashwin Vasavada, Christopher R. Webster, Albert Yen

NASA Johnson Space Center (JSC)
Paul Douglas Archer, Francis Cucinotta, John H. Jones, Douglas Ming, Richard V. Morris, Paul Niles, Elizabeth Rampe

Nolan Engineering
Thomas Nolan

Oregon State University
Martin Fisk

Piezo Energy Technologies
Leon Radziemski

Planetary Science Institute
Bruce Barraclough, Steve Bender, Daniel Berman, Eldar Noe Dobrea, Robert Tokar, David Vaniman, Rebecca M. E. Williams, Aileen Yingst

Princeton University
Kevin Lewis

Rensselaer Polytechnic Institute (RPI)
Laurie Leshin

Retired
Timothy Cleghorn, Wesley Huntress, Gérard Manhès

Salish Kootenai College
Judy Hudgins, Timothy Olson, Noel Stewart

Search for Extraterrestrial Intelligence Institute (SETI I)
Philippe Sarrazin

Smithsonian Institution
John Grant, Edward Vicenzi, Sharon A. Wilson

Southwest Research Institute (SwRI)
Mark Bullock, Bent Ehresmann, Victoria Hamilton, Donald Hassler, Joseph Peterson, Scot Rafkin, Cary Zeitlin

Space Research Institute
Fedor Fedosov, Dmitry Golovin, Natalya Karpushkina, Alexander Kozyrev, Maxim Litvak, Alexey Malakhov, Igor Mitrofanov, Maxim Mokrousov, Sergey Nikiforov, Vasily Prokhorov, Anton Sanin, Vladislav Tretyakov, Alexey Varenikov, Andrey Vostrukhin, Ruslan Kuzmin

Space Science Institute (SSI)
Benton Clark, Michael Wolff

State University of New York (SUNY) Stony Brook
Scott McLennan

Swiss Space Office
Oliver Botta

TechSource
Darrell Drake

Texas A&M
Keri Bean, Mark Lemmon

The Open University
Susanne P. Schwenzer

United States Geological Survey (USGS) Flagstaff
Ryan B. Anderson, Kenneth Herkenhoff, Ella Mae Lee, Robert Sucharski

Universidad de Alcalá
Miguel Ángel de Pablo Hernández, Juan José Blanco Ávalos, Miguel Ramos

Universities Space Research Association (USRA)
Andrea Jones, Myung-Hee Kim, Charles Malespin, Ianik Plante

University College London (UCL)
Jan-Peter Muller

University Nacional Autónoma de México (UNAM)
Rafael Navarro-González

University of Alabama
Ryan Ewing

University of Arizona
William Boynton, Robert Downs, Mike Fitzgibbon, Karl Harshman, Shaunna Morrison

University of California Berkeley
William Dietrich, Onno Kortmann, Marisa Palucis

University of California Davis
Dawn Y. Sumner, Amy Williams

University of California San Diego
Günter Lugmair

University of California San Francisco
Michael A. Wilson

University of California Santa Cruz
David Rubin

University of Colorado Boulder
Bruce Jakosky

University of Copenhagen
Tonci Balic-Zunic, Jens Frydenvang, Jaqueline Kløvgaard Jensen, Kjartan Kinch, Asmus Koefoed, Morten Bo Madsen, Susan Louise Svane Stipp

University of Guelph
Nick Boyd, John L. Campbell, Ralf Gellert, Glynis Perrett, Irina Pradler, Scott VanBommel

University of Hawai'i at Manoa
Samantha Jacob, Tobias Owen, Scott Rowland

University of Helsinki
Evgeny Atlaskin, Hannu Savijärvi

University of Kiel
Eckart Boehm, Stephan Böttcher, Sönke Burmeister, Jingnan Guo, Jan Köhler, César Martín García, Reinhold Mueller-Mellin, Robert Wimmer-Schweingruber

University of Leicester
John C. Bridges

University of Maryland
Timothy McConnochie

University of Maryland Baltimore County
Mehdi Benna, Heather Franz

University of Maryland College Park
Hannah Bower, Anna Brunner

University of Massachusetts
Hannah Blau, Thomas Boucher, Marco Carmosino

University of Michigan Ann Arbor
Sushil Atreya, Harvey Elliott, Douglas Halleaux, Nilton Rennó, Michael Wong

University of Minnesota
Robert Pepin

University of New Brunswick
Beverley Elliott, John Spray, Lucy Thompson

University of New Mexico
Suzanne Gordon, Horton Newsom, Ann Ollila, Joshua Williams

University of Queensland
Paulo Vasconcelos

University of Saskatchewan
Jennifer Bentz

University of Southern California (USC)
Kenneth Nealson, Radu Popa

University of Tennessee Knoxville
Linda C. Kah, Jeffrey Moersch, Christopher Tate

University of Texas at Austin
Mackenzie Day, Gary Kocurek

University of Washington Seattle
Bernard Hallet, Ronald Sletten

University of Western Ontario
Raymond Francis, Emily McCullough

University of Winnipeg
Ed Cloutis

Utrecht University
Inge Loes ten Kate

Vernadsky Institute
Ruslan Kuzmin

Washington University in St. Louis (WUSTL)
Raymond Arvidson, Abigail Fraeman, Daniel Scholes, Susan Slavney, Thomas Stein, Jennifer Ward

Western University
Jeffrey Berger

York University
John E. Moores

References and Notes

1. J. P. Grotzinger *et al*., Mars Science Laboratory: First 100 sols of geologic and geochemical exploration from Bradbury Landing to Glenelg. *Lunar Planet. Sci. Conf. 44*, abstract 1259 (2013).

2. R. Gellert *et al*., Initial MSL APXS activities and observations at Gale Crater, Mars. *Lunar. Planet Sci. Conf. 44*, abstract 1432 (2013).

3. A. Cousin *et al*., ChemCam analysis of Jake Matijevic, Gale Crater. *Lunar. Planet Sci. Conf. 44*, abstract 1409 (2013).

4. M. E. Minitti *et al*., Mars Hand Lens Imager (MAHLI) observations of rocks at Curiosity's field site. *Lunar. Planet Sci. Conf. 44*, abstract 2186 (2013).

5. W. Cross, J. P. Iddings, L. V. Pirsson, H. S. Washington, *Quantitative Classification of Igneous Rocks* (Univ. of Chicago Press, Chicago, 1903).

6. M. Wadhwa, Redox conditions on small bodies, the Moon and Mars. *Rev. Mineral. Geochem.* **68**, 493–510 (2008). doi:10.2138/rmg.2008.68.17

7. J. Tuff, J. Wade, B. J. Wood, Volcanism on Mars controlled by early oxidation of the upper mantle. *Nature* **498**, 342–345 (2013). Medline doi:10.1038/nature12225

8. J. M. Rhodes, Geochemical stratigraphy of lava flows sampled by the Hawaiian Scientific Drilling Project. *J. Geophys. Res.* **101**, 11729–11746 (1996). doi:10.1029/95JB03704

9. C. Meyer, The Martian Meteorite Compendium (2012); http://curator.jsc.nasa.gov/antmet/mmc/index.cfm.

10. R. Gellert, R. Rieder, J. Brückner, B. C. Clark, G. Dreibus, G. Klingelhöfer, G. Lugmair, D. W. Ming, H. Wänke, A. Yen, J. Zipfel, S. W. Squyres, Alpha Particle X-ray Spectrometer (APXS): Results from Gusev crater and calibration report. *J. Geophys. Res.* **111**, E02S05 (2006). doi:10.1029/2005JE002555

11. H. Wänke, J. Brückner, G. Dreibus, R. Rieder, I. Ryabchikov, Chemical composition of rocks and soils at the Pathfinder site. *Space Sci. Rev.* **96**, 317–330 (2001). doi:10.1023/A:1011961725645

12. C. N. Foley, T. E. Economou, R. N. Clayton, W. Dietrich, Calibration of the Mars Pathfinder Alpha Proton X-ray Spectrometer. *J. Geophys. Res.* **108**, 8095 (2003). doi:10.1029/2002JE002018

13. A. Harker, *The Tertiary Igneous Rocks of Skye*. *Memoirs of the Geological Survey of the United Kingdom* (James Hedderwick and Sons, Glasgow, 1904).

14. I. D. Muir, C. E. Tilley, Mugearites and their place in alkali igneous rock series. *J. Geol.* **69**, 186–203 (1961).

15. I. S. E. Carmichael, F. J. Turner, J. Verhoogen, *Igneous Petrology* (McGraw-Hill, New York, 1974).

16. M. Wilson, *Igneous Petrogenesis* (Unwin Hyman, London, 1989).

17. R. V. Morris, G. Klingelhöfer, C. Schröder, I. Fleischer, D. W. Ming, A. S. Yen, R. Gellert, R. E. Arvidson, D. S. Rodionov, L. S. Crumpler, B. C. Clark, B. A. Cohen, T. J. McCoy,

D. W. Mittlefehldt, M. E. Schmidt, P. A. de Souza Jr., S. W. Squyres, Iron mineralogy and aqueous alteration from Husband Hill through Home Plate at Gusev crater, Mars: Results from the Mössbauer instrument on the Spirit Mars Exploration Rover. *J. Geophys. Res.* **113**, E12S42 (2008). doi:10.1029/2008JE003201

18. V. Sautter, A. Jambon, O. Boudouma, Cl-amphibole in the nakhlite MIL 03346: Evidence for sediment contamination in a martian meteorite. *Earth Planet. Sci. Lett.* **252**, 45–55 (2006). doi:10.1016/j.epsl.2006.09.024

19. J. M. D. Day, L. A. Taylor, C. Floss, H. Y. McSween Jr., Petrology and chemistry of ML 03346 and its significance in understanding the petrogenesis of nakhlites on Mars. *Meteorit. Planet. Sci.* **41**, 581–606 (2006). doi:10.1111/j.1945-5100.2006.tb00484.x

20. A. H. Treiman, The parent magma of the Nakhla (SNC) meteorite, inferred from magmatic inclusions. *Geochim. Cosmochim. Acta* **57**, 4753–4767 (1993). doi:10.1016/0016-7037(93)90198-6

21. H. Y. McSween Jr., G. J. Taylor, M. B. Wyatt, Elemental composition of the martian crust. *Science* **324**, 736–739 (2009). doi:10.1126/science.1165871

22. A. S. Yen, D. W. Mittlefehldt, S. M. McLennan, R. Gellert, J. F. Bell III, H. Y. McSween Jr., D. W. Ming, T. J. McCoy, R. V. Morris, M. Golombek, T. Economou, M. B. Madsen, T. Wdowiak, B. C. Clark, B. L. Jolliff, C. Schröder, J. Brückner, J. Zipfel, S. W. Squyres, Nickel on Mars: Constraints on meteoritic material at the surface. *J. Geophys. Res.* **111**, E12S11 (2006). doi:10.1029/2006JE002797

23. T. N. Irvine, W. R. A. Baragar, A guide to the chemical classification of the common volcanic rocks. *Can. J. Earth Sci.* **8**, 523–548 (1971). doi:10.1139/e71-055

24. T. Usui, H. Y. McSween Jr., B. C. Clark III, Petrogenesis of high-phosphorus Wishstone Class rocks in Gusev crater, Mars. *J. Geophys. Res.* **113**, E12S44 (2008). doi:10.1029/2008JE003225

25. Georoc database; http://georoc.mpch-mainz.gwdg.de/georoc/.

26. H. Y. McSween Jr., What have we learned about Mars from SNC meteorites. *Meteoritics* **29**, 757–779 (1994). doi:10.1111/j.1945-5100.1994.tb01092.x

27. A. Ruzicka, G. A. Snyder, L. A. Taylor, Comparative geochemistry of basalts from the Moon, Earth, HED asteroid, and Mars: Implications for the origin of the Moon. *Geochim. Cosmochim. Acta* **65**, 979–997 (2001). doi:10.1016/S0016-7037(00)00599-8

28. J. Filiberto, Similarities between the shergottites and terrestrial ferropicrites. *Icarus* **197**, 52–59 (2008). doi:10.1016/j.icarus.2008.04.016

29. E. Stolper, H. Y. McSween Jr., J. F. Hays, A petrogenetic model of the relationships among achondritic meteorites. *Geochim. Cosmochim. Acta* **43**, 589–602 (1979). doi:10.1016/0016-7037(79)90167-4

30. H. Wänke, G. Dreibus, Chemical composition and accretion history of terrestrial planets. *Philos. Trans. R. Soc. London Ser. A* **325**, 545–557 (1988). doi:10.1098/rsta.1988.0067

31. J. Karner, J. J. Papike, C. K. Shearer, Olivine from planetary basalts: Chemical signatures that indicate planetary parentage and those that record igneous setting and process. *Am. Mineral.* **88**, 806–816 (2003).

32. J. Karner, J. J. Papike, C. K. Shearer, Comparative planetary mineralogy: Pyroxene major- and minor-element chemistry and partitioning of vanadium between pyroxene and melt in planetary basalts. *Am. Mineral.* **91**, 1574–1582 (2006). doi:10.2138/am.2006.2103

33. A. Lacroix, Les lavas à haüyne d'Auvergne et leurs enclaves homoeogènes. *Comptes Rendus* **CLXIV**, 581–587 (1917).

34. J. Andújar, F. Costa, J. Martí, J. A. Wolff, M. R. Carroll, Experimental constraints on pre-eruptive conditions of phonolitic magma from caldera-forming El Abrigo eruption, Tenerife (Canary Islands). *Chem. Geol.* **257**, 173–191 (2008). doi:10.1016/j.chemgeo.2008.08.012

35. J. F. G. Wilkinson, R. A. Binns, Hawaiite of high pressure origin from northeastern New South Wales. *Nature* **222**, 553–555 (1969). doi:10.1038/222553a0

36. A. J. Stolz, Garnet websterites and associated ultramamfic inclusions from a nepheline mugearite in the Walcha area, New South Wales, Australia. *Mineral. Mag.* **48**, 167–179 (1984). doi:10.1180/minmag.1984.048.347.02

37. D. H. Green, A. D. Edgar, P. Beasley, E. Kiss, N. G. Ware, Upper mantle source for some hawaiites, mugearites and benmoreites. *Contrib. Mineral. Petrol.* **48**, 33–43 (1974). doi:10.1007/BF00399108

38. G. J. Ablay, M. R. Carroll, M. R. Palmer, J. Martí, R. S. J. Sparks, Basanite-phonolite lineages of the Teide-Pico volcanic complex, Tenerife, Canaray Islands. *J. Petrol.* **39**, 905–936 (1998). doi:10.1093/petroj/39.5.905

39. P. M. Smith, P. D. Asimow, Adiabat_1ph: A new public front-end to the MELTS, pMELTS, and pHMELTS models. *Geochem. Geophys. Geosyst.* **6**, Q02004 (2005). doi:10.1029/2004GC000816

40. M. S. Ghiorso, R. O. Sack, Chemical mass transfer in magmatic processes. IV. A revised and internally consistent thermodynamic model for the interpolation and extrapolation of liquid-solid equilibria. *Contrib. Mineral. Petrol.* **119**, 197–212 (1995). doi:10.1007/BF00307281

41. H. S. Yoder, C. E. Tilley, Origin of basaltic magmas: An experimental study of natural and synthetic rock systems. *J. Petrol.* **3**, 342–532 (1962). doi:10.1093/petrology/3.3.342

42. D. C. Presnall, S. A. Dixon, J. R. Dixon, T. H. O'Donnell, N. L. Brenner, R. L. Schrock, D. W. Dycus, Liquidus phase relations on the join diopside-forsterite-anorthite from 1-atm to 20 kbar: Their bearing on the generation and crystallization of basaltic magma. *Contrib. Mineral. Petrol.* **66**, 203–220 (1978). doi:10.1007/BF00372159

43. D. H. Eggler, Water-saturated and undersaturated melting relations in a Paricutin andesite and an estimate of water content in the natural magma. *Contrib. Mineral. Petrol.* **34**, 261–271 (1972). doi:10.1007/BF00373757

44. P. J. Wyllie, Magmas and volatile components. *Am. Mineral.* **64**, 469–500 (1979).

45. G. J. Ablay, G. G. J. Ernst, J. Marti, R. S. J. Sparks, The ~2ka subplinian eruption of Montana Blanca, Tenerife. *Bull. Volcanol.* **57**, 337–355 (1995).

46. C. Beier, K. M. Haase, T. H. Hansteen, Magma evolution of the Sete Cidades volcano, São Miguel, Azores. *J. Petrol.* **47**, 1375–1411 (2006). doi:10.1093/petrology/egl014

47. J. C. Dann, A. H. Holzheid, T. L. Grove, H. Y. McSween Jr., Phase equilibria of the Shergotty meteorite: Constraints on pre-eruptive water contents of martian magmas and fractional crystallization under hydrous conditions. *Meteorit. Planet. Sci.* **36**, 793–806 (2001). doi:10.1111/j.1945-5100.2001.tb01917.x

48. H. Nekvasil, J. Filiberto, F. M. McCubbin, D. H. Lindsley, Alkalic parental magmas for chassignites? *Meteorit. Planet. Sci.* **42**, 979–992 (2007). doi:10.1111/j.1945-5100.2007.tb01145.x

49. M. C. Johnson, M. J. Rutherford, P. C. Hess, Chassigny petrogenesis: Melt compositions, intersive parameters, and water contents of martian (?) magmas. *Geochim. Cosmochim. Acta* **55**, 349–366 (1991). doi:10.1016/0016-7037(91)90423-3

50. F. M. McCubbin, A. Smirnov, H. Nekvasil, J. Wang, E. Hauri, D. H. Lindsley, Hydrous magmatism on Mars: A source of water for the surface and subsurface during the Amazonian. *Earth Planet. Sci. Lett.* **292**, 132–138 (2010). doi:10.1016/j.epsl.2010.01.028

51. J. Filiberto, A. H. Treiman, Martian magmas contained abundant chlorine, but little water. *Geology* **37**, 1087–1090 (2009). doi:10.1130/G30488A.1

52. D. R. Baker, M. Alletti, Fluid saturation and volatile partitioning between melts and hydrous fluids in crustal magmatic systems: The contribution of experimental measurements and solubility models. *Earth Sci. Rev.* **114**, 298–324 (2012). doi:10.1016/j.earscirev.2012.06.005

53. M. R. Carroll, J. D. Webster, Solubilities of sulfur, noble gases, nitrogen, chlorine, and fluorine in magmas. *Rev. Mineral.* **30**, 231–279 (1994).

54. P. J. Wyllie, O. F. Tuttle, Experimental investigations of silicate systems containing two volatile components. Part III. The effects of SO_3, P_2O_5, HCl, and Li_2O, in addition to H_2O, on the melting temperatures of albite and granite. *Am. J. Sci.* **262**, 930–939 (1964). doi:10.2475/ajs.262.7.930

55. A. D. Edgar, in *Alkaline Igneous Rocks*, J. G. Fitton, B. G. J. Upton, Eds. (Geological Society of London, London, 1987), pp. 29–52.

56. D. H. Green, T. J. Falloon, W. R. Taylor, in *Magmatic Processes: Physiochemical Principles*, B. O. Mysen, Ed. (The Geochemical Society, University Park, PA, 1987), pp. 139–154.

57. R. Dasgupta, M. M. Hirschmann, N. D. Smith, Partial melting experiments of peridotite + CO_2 at 3 GPa and genesis of alkalic ocean island basalts. *J. Petrol.* **48**, 2093–2124 (2007). doi:10.1093/petrology/egm053

58. F. E. Lloyd, D. K. Bailey, Light element metasomatism of the continental mantle: The evidence and the consequences. *Phys. Chem. Earth* **9**, 389–416 (1975). doi:10.1016/0079-1946(75)90030-0

59. M. Menzies, V. Rama Murthy, Mantle metasomatism as a precursor to the genesis of alkaline magmas—Isotopic evidence. *Am. J. Sci.* **280-A**, 622–638 (1980).

60. S. Pilet, M. B. Baker, E. M. Stolper, Metasomatized lithosphere and the origin of alkaline lavas. *Science* **320**, 916–919 (2008). doi:10.1126/science.1156563

61. S. Keshav, G. H. Gudfinnsson, G. Sen, Y. W. Fei, High-pressure melting experiments on garnet clinopyroxenite and the alkalic to tholeiitic transition in ocean-island basalts. *Earth Planet. Sci. Lett.* **223**, 365–379 (2004). doi:10.1016/j.epsl.2004.04.029

62. T. Kogiso, M. M. Hirschmann, D. J. Frost, High-pressure partial melting of garnet pyroxenite: Possible mafic lithologies in the source of ocean island basalts. *Earth Planet. Sci. Lett.* **216**, 603–617 (2003). doi:10.1016/S0012-821X(03)00538-7

63. M. E. Schmidt, T. J. McCoy, The evolution of a heterogeneous Martian mantle: Clues from K, P, Ti, Cr, and Ni variations in Gusev basalts and shergottite meteorites. *Earth Planet. Sci. Lett.* **296**, 67–77 (2010). doi:10.1016/j.epsl.2010.04.046

64. H. Y. McSween, Jr., S. W. Ruff, R. V. Morris, J. F. Bell III, K. Herkenhoff, R. Gellert, K. R. Stockstill, L. L. Tornabene, S. W. Squyres, J. A. Crisp, P. R. Christensen, T. J. McCoy, D. W. Mittlefehldt, M. Schmidt, Alkaline volcanic rocks from the Columbia Hills, Gusev crater, Mars. *J. Geophys. Res.* **111**, E09S91 (2006). doi:10.1029/2006JE002698

65. G. Dreibus, H. Wänke, Volatiles on Earth and Mars: A comparison. *Icarus* **71**, 225–240 (1987). doi:10.1016/0019-1035(87)90148-5

66. G. J. Taylor *et al*., Bulk composition and early differentiation of Mars. *J. Geophys. Res.* **111**, E03S10 (2006).

67. K. Lodders, B. Fegley Jr., An oxygen isotope model for the composition of Mars. *Icarus* **126**, 373–394 (1997). doi:10.1006/icar.1996.5653

68. S. M. McLennan, Large-ion lithophile element fractionation during the early differentiation of Mars and the composition of the Martian primitive mantle. *Meteorit. Planet. Sci.* **38**, 895–904 (2003). doi:10.1111/j.1945-5100.2003.tb00286.x

69. A. H. Treiman, Chemical compositions of martian basalts (shergottites): Some inferences on basalt formation, mantle metasomatism, and differentiation in Mars. *Meteorit. Planet. Sci.* **38**, 1849–1864 (2003). doi:10.1111/j.1945-5100.2003.tb00019.x

70. J. D. Winter, *An Introduction to Igneous and Metamorphic Petrology* (Prentice Hall, Upper Saddle River, NJ, 2010).

71. M. E. Schmidt *et al*., APXS of first rocks encountered by Curiosity in Gale Crater: Geochemical diversity and volatile element (K and Zn) enrichment. *Lunar Planet. Sci. Conf. 44*, abstract 1278 (2013).

72. R. W. Le Maitre, Ed., *Igneous Rocks: A Classification and Glossary of Terms* (Cambridge Univ. Press, Cambridge, ed. 2, 2002).

73. H. C. Aoudjehane, G. Avice, J. A. Barrat, O. Boudouma, G. Chen, M. J. Duke, I. A. Franchi, J. Gattacceca, M. M. Grady, R. C. Greenwood, C. D. Herd, R. Hewins, A. Jambon, B. Marty, P. Rochette, C. L. Smith, V. Sautter, A. Verchovsky, P. Weber, B. Zanda, Tissint

martian meteorite: A fresh look at the interior, surface, and atmosphere of Mars. *Science* **338**, 785–788 (2012). doi:10.1126/science.1224514

74. C. B. Agee, N. V. Wilson, F. M. McCubbin, K. Ziegler, V. J. Polyak, Z. D. Sharp, Y. Asmerom, M. H. Nunn, R. Shaheen, M. H. Thiemens, A. Steele, M. L. Fogel, R. Bowden, M. Glamoclija, Z. Zhang, S. M. Elardo, Unique meteorite from early Amazonian Mars: Water-rich basaltic breccia Northwest Africa 7034. *Science* **339**, 780–785 (2013). doi:10.1126/science.1228858

75. D. W. Ming, R. Gellert, R. V. Morris, R. E. Arvidson, J. Brückner, B. C. Clark, B. A. Cohen, C. d'Uston, T. Economou, I. Fleischer, G. Klingelhöfer, T. J. McCoy, D. W. Mittlefehldt, M. E. Schmidt, C. Schröder, S. W. Squyres, E. Tréguier, A. S. Yen, J. Zipfel, Geochemical properties of rocks and soils in Gusev crater, Mars: Results of the Alpha Particle X-ray Spectrometer from Cumberland Ridge to Home Plate. *J. Geophys. Res.* **113**, E12S39 (2008). doi:10.1029/2008JE003195

76. R. Rieder, R. Gellert, R. C. Anderson, J. Brückner, B. C. Clark, G. Dreibus, T. Economou, G. Klingelhöfer, G. W. Lugmair, D. W. Ming, S. W. Squyres, C. d'Uston, H. Wänke, A. Yen, J. Zipfel, Chemistry of rocks and soils at Meridiani Planum from the Alpha Particle X-ray Spectrometer. *Science* **306**, 1746–1749 (2004). doi:10.1126/science.1104358

77. S. W. Squyres, O. Aharonson, B. C. Clark, B. A. Cohen, L. Crumpler, P. A. de Souza, W. H. Farrand, R. Gellert, J. Grant, J. P. Grotzinger, A. F. Haldemann, J. R. Johnson, G. Klingelhöfer, K. W. Lewis, R. Li, T. McCoy, A. S. McEwen, H. Y. McSween, D. W. Ming, J. M. Moore, R. V. Morris, T. J. Parker, J. W. Rice Jr., S. Ruff, M. Schmidt, C. Schröder, L. A. Soderblom, A. Yen, Pyroclastic activity at Home Plate in Gusev crater, Mars. *Science* **316**, 738–742 (2007). doi:10.1126/science.1139045

78. R. H. Hewins *et al*., Northwest Africa 7533, an impact breccia from Mars. *Lunar Planet. Sci. Conf. 44*, abstract 2385 (2013).

79. M. Humayun, B. Zanda, R. H. Hewins, C. Göpel, Composition of Northwest Africa 7533: Implications for the origin of martian soils and crust. *Lunar Planet. Sci. Conf. 44*, abstract 1429 (2013).

80. A. K. Matzen, M. B. Baker, J. R. Beckett, E. M. Stolper, Fe-Mg partitioning between olivine and high-magnesian melts and the nature of Hawaiian parental liquids. *J. Petrol.* **52**, 1243–1263 (2011). doi:10.1093/petrology/egq089

81. J. Filiberto, R. Dasgupta, Fe^{+2}-Mg partitioning between olivine and basaltic melts: Applications to genesis of olivine-phyric Shergottites and conditions of melting in the Martian interior. *Earth Planet. Sci. Lett.* **304**, 527–537 (2011). doi:10.1016/j.epsl.2011.02.029

82. E. M. Stolper *et al*., The petrochemistry of Jake_M: A martian mugearite. *Lunar Planet. Sci. Conf. 44*, abstract 1685 (2013).

83. E. M. Stolper *et al*., The petrochemistry of Jake_M: A martian mugearite. *Mineral. Mag.* **77**, 2269 (2013).

84. J. Brückner *et al*., in *The Martian Surface: Composition, Mineralogy, and Physical Properties*, J. F. Bell III, Ed. (Cambridge Univ. Press, Cambridge, 2008), pp. 58–102.

85. J. A. Hurowitz, S. M. McLennan, N. J. Tosca, R. E. Arvidson, J. R. Michalski, D. W. Ming, C. Schröder, S. W. Squyres, In situ and experimental evidence for acidic weathering of rocks and soils on Mars. *J. Geophys. Res.* **111**, E02S19 (2006). doi:10.1029/2005JE002515

86. S. Maurice, R. C. Wiens, M. Saccoccio, B. Barraclough, O. Gasnault, O. Forni, N. Mangold, D. Baratoux, S. Bender, G. Berger, J. Bernardin, M. Berthé, N. Bridges, D. Blaney, M. Bouyé, P. Caïs, B. Clark, S. Clegg, A. Cousin, D. Cremers, A. Cros, L. DeFlores, C. Derycke, B. Dingler, G. Dromart, B. Dubois, M. Dupieux, E. Durand, L. d'Uston, C. Fabre, B. Faure, A. Gaboriaud, T. Gharsa, K. Herkenhoff, E. Kan, L. Kirkland, D. Kouach, J.-L. Lacour, Y. Langevin, J. Lasue, S. Mouélic, M. Lescure, E. Lewin, D. Limonadi, G. Manhès, P. Mauchien, C. McKay, P.-Y. Meslin, Y. Michel, E. Miller, H. E. Newsom, G. Orttner, A. Paillet, L. Parès, Y. Parot, R. Pérez, P. Pinet, F. Poitrasson, B. Quertier, B. Sallé, C. Sotin, V. Sautter, H. Séran, J. J. Simmonds, J.-B. Sirven, R. Stiglich, N. Striebig, J.-J. Thocaven, M. J. Toplis, D. Vaniman, The ChemCam instrument suite on the Mars Science Laboratory (MSL) rover: Science objectives, and mast unit description. *Space Sci. Rev.* **170**, 95–166 (2012). doi:10.1007/s11214-012-9912-2

87. R. C. Wiens, S. Maurice, B. Barraclough, M. Saccoccio, W. C. Barkley, J. F. Bell, S. Bender, J. Bernardin, D. Blaney, J. Blank, M. Bouyé, N. Bridges, N. Bultman, P. Caïs, R. C. Clanton, B. Clark, S. Clegg, A. Cousin, D. Cremers, A. Cros, L. DeFlores, D. Delapp, R. Dingler, C. D'Uston, M. Darby Dyar, T. Elliott, D. Enemark, C. Fabre, M. Flores, O. Forni, O. Gasnault, T. Hale, C. Hays, K. Herkenhoff, E. Kan, L. Kirkland, D. Kouach, D. Landis, Y. Langevin, N. Lanza, F. LaRocca, J. Lasue, J. Latino, D. Limonadi, C. Lindensmith, C. Little, N. Mangold, G. Manhes, P. Mauchien, C. McKay, E. Miller, J. Mooney, R. V. Morris, L. Morrison, T. Nelson, H. Newsom, A. Ollila, M. Ott, L. Pares, R. Perez, F. Poitrasson, C. Provost, J. W. Reiter, T. Roberts, F. Romero, V. Sautter, S. Salazar, J. J. Simmonds, R. Stiglich, S. Storms, N. Striebig, J.-J. Thocaven, T. Trujillo, M. Ulibarri, D. Vaniman, N. Warner, R. Waterbury, R. Whitaker, J. Witt, B. Wong-Swanson, The ChemCam instrument suite on the Mars Science Laboratory (MSL) rover: Body unit and combined system tests. *Space Sci. Rev.* **170**, 167–227 (2012). doi:10.1007/s11214-012-9902-4

88. E. Lewin *et al*., Modal mineralogy of igneous rocks with ChemCam at Gale crater. *Lunar Planet. Sci. Conf. 44*, abstract 3102 (2013).

89. S. Maurice *et al*., Laser Induced Spectroscopy (LIBS) spot size stand-off distances with ChemCam. *Lunar Planet. Sci. Conf. 43*, abstract 2899 (2012).

90. P. Comon, Independent component analysis, a new concept? *Signal Process.* **36**, 287–314 (1994). doi:10.1016/0165-1684(94)90029-9

91. O. Forni *et al*., Component separation of OMEGA spectra with ICA. *Lunar Planet. Sci. Conf. 36*, abstract 1623 (2005).

92. J. Lasue *et al*., Partial least squares sensitivity analysis and improvements for ChemCam LIBS data anlysis on Mars. *Lunar Planet. Sci. Conf. 44*, abstract 2230 (2013).

93. L. Qin, M. Humayun, The Fe/Mn ratio in MORB and OIB determined by ICP-MS. *Geochim. Cosmochim. Acta* **72**, 1660–1677 (2008). doi:10.1016/j.gca.2008.01.012

94. M. Humayun, L. Qin, M. D. Norman, Geochemical evidence for excess iron in the mantle beneath Hawaii. *Science* **306**, 91–94 (2004). doi:10.1126/science.1101050

95. W. I. Ridley, The petrology of the Las Canada volcanoes, Tenerife, Canary Islands. *Contrib. Mineral. Petrol.* **26**, 124–160 (1970). doi:10.1007/BF00371260

96. M. M. Hirschmann, M. S. Ghiorso, L. E. Wasylenki, P. D. Asimow, E. M. Stolper, Calculation of peridotite partial melting from thermodynamic models of minerals and melts. I. Review of methods and comparison with experiments. *J. Petrol.* **39**, 1091–1115 (1998). doi:10.1093/petroj/39.6.1091

97. C. D. K. Herd, Basalts as probes of planetary interior redox state. *Rev. Mineral. Geochem.* **68**, 527–553 (2008). doi:10.2138/rmg.2008.68.19

98. Y. Bottinga, D. F. Weill, The viscosity of magmatic silicate liquids: A model calculation. *Am. J. Sci.* **272**, 438–475 (1972). doi:10.2475/ajs.272.5.438